



Western Washington University
Western CEDAR

WWU Graduate School Collection

WWU Graduate and Undergraduate Scholarship

Spring 2020

Paleomagnetic and Structural Analysis of Geothermal Drill Core from Akutan, Alaska

Molly Kathleen Johnson

Western Washington University, molli.kate@gmail.com

Follow this and additional works at: <https://cedar.wwu.edu/wwuet>



Part of the [Geology Commons](#)

Recommended Citation

Johnson, Molly Kathleen, "Paleomagnetic and Structural Analysis of Geothermal Drill Core from Akutan, Alaska" (2020). *WWU Graduate School Collection*. 964.

<https://cedar.wwu.edu/wwuet/964>

This Masters Thesis is brought to you for free and open access by the WWU Graduate and Undergraduate Scholarship at Western CEDAR. It has been accepted for inclusion in WWU Graduate School Collection by an authorized administrator of Western CEDAR. For more information, please contact westerncedar@wwu.edu.

Paleomagnetic and Structural Analysis of Geothermal Drill Core from Akutan, Alaska

By
Molly Johnson

Accepted in Partial Completion
of the Requirements for the Degree
Master of Science

ADVISORY COMMITTEE

Dr. Bernard Housen, Chair

Dr. Pete Stelling

Dr. Elizabeth Schermer

GRADUATE SCHOOL

David L. Patrick, Interim Dean

Master's Thesis

In presenting this thesis in partial fulfillment of the requirements for a master's degree at Western Washington University, I grant to Western Washington University the non-exclusive royalty-free right to archive, reproduce, distribute, and display the thesis in any and all forms, including electronic format, via any digital library mechanisms maintained by WWU.

I represent and warrant this is my original work and does not infringe or violate any rights of others. I warrant that I have obtained written permissions from the owner of any third party copyrighted material included in these files.

I acknowledge that I retain ownership rights to the copyright of this work, including but not limited to the right to use all or part of this work in future works, such as articles or books.

Library users are granted permission for individual, research and non-commercial reproduction of this work for educational purposes only. Any further digital posting of this document requires specific permission from the author.

Any copying or publication of this thesis for commercial purposes, or for financial gain, is not allowed without my written permission.

Molly Johnson

May 3rd, 2020

Paleomagnetic and Structural Analysis of Geothermal Drill Core from Akutan, Alaska

A Thesis
Presented to
The Faculty of
Western Washington University

In Partial Fulfillment
Of the Requirements for the Degree
Master of Science

by
Molly Johnson
May 2020

Abstract

Hot Springs Bay Valley (HSBV) geothermal resource area on Akutan Island, Alaska, has increased fluid output and temperature by almost a magnitude, between 1981 and 2012 (Bergfeld et al., 2014). These increases have been attributed to increased permeability along NW-SE trending faults that may have been activated during a seismic swarm in 1996. In 2010 two unoriented drill cores were collected in Hot Springs Bay geothermal resource area. In this study I reorient sections from one of the highly fractured cores with paleomagnetic data to test this model of geothermal reservoir evolution at Akutan. The core is composed of interlayered island arc volcanic rocks, volcanoclastic rocks, and shallow marine mudstones. Paleomagnetic samples were collected from the volcanic rocks. Continuous sections of the core were reoriented using the declination of the remanent magnetization (RM) as an indication of geographic north. Structure from motion software was used to create digital reconstructions of the core from photographs. The resulting core images were then flattened with a cylindrical projection into a 2D depiction of the outside of the core. The orientation of structural features and the relationships between them were measured from these projections, while the mineralogy and rake of slickenlines were determined in hand sample. Veins with slickenfibers were separated by mineralogy and the Multiple Inverse Method (MIM) (Yamaji, 2000) was employed to calculate the stress regime that produced each set of shear veins. Results suggest that NNE dipping transtensional calcite filled shear veins are the result of periodic rupture possibly caused by inflation of the volcano due to dike emplacement and represent recharge of the reservoir. NNW trending chlorite filled shear veins are the result of normal overburden pressure alternating with NNW horizontal compression and likely represent the northward migration of heated fluids to the reservoir. Cross cutting relations indicate that NE and SW dipping, NW-SE normal faults are conjugate and have ruptured repeatedly. Therefore, events like the 1996 seismic swarm, which produced NW trending surface ground cracks, have likely acted to maintain permeability throughout the lifetime of the geothermal system at Akutan. I propose that the increased fluid flow and heat output recorded by Bergfeld et al. (2014) is the result of a recharge event initiated by the rupture of NE and SW dipping structures.

Acknowledgments

This work was funded by the Western Washington University Foundation, the Geological Society of America and by the Alaska Geological Society. I would like to thank the City of Akutan and Geothermal Resources Group for providing access to the core; my committee members for their guidance; Ben Paulson for his support in creating the drill logs; Russ Burmester, Will Callebert, and Masoud Mirzaei for their support in the at the Northwest Paleomagnetism Lab; Daniel Fagerlie for writing a python script that automated the creation of digital masks; and Nathaniel VanArendonk for creating a Matlab script which plotted the depth verse strike plots; and Bret Tobin and Paige Knapp for providing thin sections.

To my family, thank you for cheering me on, buying me groceries, and taking my late-night calls. You make me who I am, and I love you all. Thank you to my cohort who pushed me out of my bounds and encouraged me to be better. And finally, I owe the completion of this work to my partner, Jeremy Rosen, without whom the road would've been far too dark. Thank you for believing in me.

Table of Contents

Abstract.....	iv
Acknowledgements.....	v
List of Tables and Figures.....	vii
1. Introduction.....	1
2. Geologic Context	1
3. Paleomagnetic Investigation	4
3.1 Rock Magnetism	4
3.1.1 Rock Magnetism Methods	5
3.1.2 Rock Magnetism Results	6
3.1.3 Rock Magnetism Implications	7
3.2 Paleomagnetic Directions	8
3.2.1 Demagnetization Methods	8
3.2.2 Demagnetization Results	10
3.2.3 Interpretation of Paleomagnetic Directions	13
4. Structural Investigation.....	14
4.1 Core Analysis.....	15
4.1.1 Core Analysis Methods.....	15
4.1.2 Core Analysis Results	16
4.1.3 Implications of Reoriented Structures and Mineralogy	18
4.2 Paleostress Inversion	19
4.2.1 Paleostress Inversion Methods.....	19

4.2.2 Paleostress Inversion Results	20
4.2.3 Interpretation of Inverted Stress States	22
5. Discussion and Summary	23
Works Cited	27
Tables	30
Figures	34
Appendix A	63

List of Tables

Table 1: Results of demagnetization for selected sites	30
Table 2: Inclination, declination, and reorientation error of site means	31
Table 3: Principal stress directions from MIM analysis	32
Table A1: Representative sample masses	33

List of Figures

Figure 1: Reference map of Akutan and Hot Springs Bay Valley	34
Figure 2: Hysteresis loops for representative samples	35
Figure 3: Unmixed IRM curves for representative samples	36
Figure 4: Day plot of representative samples.	39
Figure 5: Position of paleomagnetic samples relative to the false north mark (N')	40
Figure 6: Core log	41
Figure 7: Representative Zijderveld plots of tuff samples	44
Figure 8: Representative Zijderveld plots of andesite samples	45
Figure 9: Representative Zijderveld plots of basalt samples	47
Figure 10: Stereoplot of selected paleomagnetic directions, site means, and reorientation error	48

Figure 11: Zijdeveld plot for andesite and basalt flows in site 287.1-299.6 m site	49
Figure 12: Comparison of calculated and measured dip and strike data	50
Figure 13: Stereonets of poles to planes for unoriented and reoriented structural data.....	50
Figure 14: Stereonets and depth plots for fractures, veins, and vein widths	51
Figure 15: Micrograph of poly and monomineralic veins within reoriented core segments	52
Figure 16: Stereonets and depth plots for vein mineralogy and cross cutting relations	53
Figure 17: Stereonets of veins with slickenlines.....	54
Figure 18: Stereonets of veins with multiple slickenlines	55
Figure 19: Results of MIM analysis grouped by orientation	56
Figure 20: Results of MIM analysis for all shear veins	57
Figure 21: Results of MIM analysis for chlorite ± calcite filled shear veins.....	59
Figure 22: Results of MIM analysis for calcite + chlorite filled shear veins.....	60
Figure 23: Results of MIM analysis for calcite - chlorite filled shear veins.....	61
Figure 24: Map of Akutan and Hot Springs Bay Valley	62

1. Introduction

The City of Akutan and adjacent Trident Seafoods processing plant on Akutan Island (Figure 1B) would greatly benefit from a local source of clean energy. The City of Akutan and Trident Seafood's current energy needs are being met by burning 4.3 million gallons of diesel fuel annually (Kolker et al., 2011). In 2011 residential electricity rates in Akutan were 0.32 \$/kWh; 167% greater than the national average (Fay et al., 2013). The electrical need here could be met by establishing a geothermal power plant in the Hot Springs Bay Valley (HSBV) geothermal resource area, which would add valuable infrastructure to the island and eastern Aleutians, help the community become more energy independent, and diversify the job market.

The Aleutian Island chain, and Akutan Island in particular (Figure 1A), has high potential for geothermal power production (Motyka et al., 1993; Kolker et al., 2012; Stelling et al., 2015). Previous geochemical studies (Bergfeld et al., 2014; Stelling et al., 2015) and downhole measurements of two slim wells (Kolker et al., 2011) have confirmed enough reservoir heat to produce 2-3 MWe or more from the resource (Stelling et al., 2015). Furthermore, Bergfeld et al., (2014) noted a 134% increase in discharge of the thermal creek and increased temperatures resulting in a 29MW thermal output for the hot springs, which is nearly an order of magnitude greater than previous studies (Motyka et al., 1988). These increases reflect both an increase in heat flow and an increase in permeability of the system between 1981 and 2012. Bergfeld et al., (2014) postulated that rupture of a system of NW-SE striking faults during the seismic swarm in 1996 could explain the increased permeability and noted that the increased heat output is particularly long lasting if their hypothesis is correct. The primary goal of this work is to determine the orientation of permeable structural features in the subsurface of the HSBV geothermal resource, and therefore test Bergfeld's hypothesis by determining if the geometry of these features are compatible with the NW-SE striking faults.

2. Geologic Context

Akutan Island is one of the easternmost Aleutian Islands and in the central portion of the Aleutian volcanic arc formed from the northwestward subduction of the Pacific plate under the North American plate. The active volcano dominates the western half of the island, and the eastern half of the island is composed of glacially scoured remnants of ancient volcanic activity (Figure 1). Romick et al. (1990) separated the rock units on Akutan into three broad categories. The oldest

rocks on the island are the Hot Springs volcanics (HSV), overlain by the ancestral Akutan volcanics (AKV), and the modern Akutan volcanics (MOD) with the most recent lava flows in the north of the island. The AKV and MOD are separated by an angular unconformity (Romick et al., 1990). The AKV are cut by dikes of MOD which mostly parallel the ridges that extend out from Akutan volcano (Byers and Barth, 1953). Akutan has been one of the most active volcanoes in the region for decades (Finch, 1935; Miller et al., 1998). Based on historical records, major activity on the volcano occurs approximately every 20 years (Byers and Barth, 1953), the most recent of which was in 1996, which has been attributed to the emplacement of a shallow dike (Lu et al., 2005). There are two geothermal systems on Akutan (Motyka et al., 1993), one in the summit crater and one on the flank of the volcano in HSBV.

The HSBV is a glacially carved valley on the eastern side of the island. The upper valley is oriented NW/SE and the lower valley is oriented NE/SW. The two valleys meet in the southwest, forming an approximately 90° bend (Figure 1C) suggesting that the glacier's path may have been structurally controlled. As on the rest of the island, fault scarps, fractures, dikes and lineaments in HSBV have three main orientations: NW/SE, E/W, and NE/SW (Figure 1C) (Richter et al., 1998; Stelling et al., 2015). A prominent SW dipping normal fault cuts through HSBV (Richter et al. 1998). Most faults mapped in HSBV have dips to the south and SW and show a down-to-the-south dip slip or oblique slip motion with dip angles between 50° and 90°, however nearly a third of the faults mapped throughout the island do not have dip direction constrained. Joints also dip between 50° and near vertical, but the dip direction is bimodal to the north and south (Stelling et al., 2015).

The seismic swarm of 1996 consisted of >3000 earthquakes ($M_{\max}=5.1$) that reactivated WNW-ESE striking faults south of HSBV and across the island (Lu et al., 2005). The change in ground surface morphology (60 cm of uplift) during the 1996 seismic event is consistent with the emplacement of a vertical dike as shallow as 0.4 km beneath the northwest flank of Akutan volcano oriented parallel to ground cracks striking N70W (Lu et al., 2005). Inflation of the northern flank by 5 mm/yr from 1992-1995 and by 20mm/yr from 1995-1996 has been interpreted to be the result of magma injection. Subsidence of the volcano's northwest flank in 1996-1997 by about 20mm may be due to the cooling and degassing of the intrusion (Lu et al., 2005). The deepening of seismicity through time (1-5km from 1996-2004, 0-3km in 2005, 4km from 2008-2009) at this location is attributed to cooling of deeper portions of the dike and surrounding rocks (Syracuse et

al., 2015). The documented subsidence on the eastern flank of the volcano from 1994-1997 has been attributed to depressurization of the hydrothermal field facilitated by movement along normal faults (Lu et al., 2005). As of 2015 there has been very little seismicity in HSBV since the end of the 1996 swarm (Syracuse et al., 2015).

The HSBV hydrothermal system hosts a fumarole field at the head of the upper valley and a string of hot springs extending ~1 mile along the northern wall of the lower valley (Figure 1). The fumaroles and the hot springs are likely connected and stem from the same deep reservoir. The current conceptual model by Stelling et al., (2015) is based on gas geochemistry, silica and cation geothermometry, magnetotelluric surveys, and down-hole temperature measurements. According to this model there is a high temperature upflow under the fumaroles that bifurcates into a lower temperature outflow daylighting at the hot springs. Kolker et al. (2012) proposed two different flow paths for the outflow, one following HSBV to the south, and the other curving north under Mt. Formidable just north of HSBV (Figure 1C). A geochemical study of the hot springs (Bergfeld et al., 2014) reported a heat output of ~29MW, which is about an order of magnitude higher than studies done in 1981 (Motyka et al., 1993). Additionally, Bergfeld et al. (2014) reported a 20-25% increase in the flow of thermal streams, a 10° C increase in temperature of thermal springs as well as substantial increases in most of the individual dissolved solids which combined indicate an increase in hydrothermal activity. Bergfeld et al. (2014) suggest this increase in heat and discharge is the result of increased fracture density and dilation along the WNW-ESE oriented normal fault between the hot springs and the fumaroles that was re-activated during the 1996 seismic swarm.

In 2010, two thermal gradient wells were drilled in Hot Springs Bay Valley on Akutan Island as part of a geothermal exploration project (Kolker et al., 2012; Stelling et al., 2015). Both wells were recovered entirely as unoriented core, with variable degrees of fracturing. Well TG-2 is 254 m (833 ft.) deep, located on the northern side of the lower valley near the hot springs (Figure 1C). Approximately 90% of the interval drilled at TG-2 was recovered as core. Well TG-4 is 457.2 m (1500 ft.) deep and located along the southwestern valley wall at the confluence of the upper and lower valleys (Kolker et al., 2011), with core recovery of ~98% (Figure 1C). Well TG-2 was drilled next to the hot springs to intercept the outflow, and TG-4 was drilled at the confluence of the upper and lower valleys where the three major orientations of faults intersect. The core from

TG-4 is therefore well suited to test models of reservoir evolution. The cores consist of interbedded basalt and andesite lavas, andesitic and dacitic tuffs, and mass wasting deposits. Similarities between lithologic units and variable alteration have made traditional stratigraphy unsuccessful. The hydrothermal alteration can take the form of high-density hairline veining, mottled white and green mineralization in the matrix of mass wasting deposits, or pale green chlorite and clay mineralization around fracture planes, veins, and lithologic contacts that extend several centimeters into the rock. Areas of high permeability are often associated with the brecciated tops of vesicular basalt and andesite flows or with hydrothermally altered and fractured tuffs (Kolker et al., 2012; Stelling, 2015).

3. Paleomagnetic Investigation

Reorientation of segments from TG-4 was done using the declination of remnant magnetism (RM) in the core as an indicator of geographic north. Using RM is an inexpensive and proven technique for orienting already-drilled core (Fuller, 1969) and has been used widely in such varied studies as petroleum exploration (Allerton et al., 1995; Hailwood and Ding, 1995), by the Ocean Drilling Program to study the structure of subduction wedges (Hill et al., 1993), and to establish magnetostratigraphic sections for late-Triassic to early Jurassic volcanic rocks (Kent et al., 1995). Yet there are several challenges employing this method at Akutan. The high latitude of Akutan results in a very steep inclination of the magnetic signal (72° in the modern field), and therefore the declination signal has a high degree of intrinsic error. Furthermore, the magnetic signal could have been overprinted by the drilling of the core (Hailwood and Ding, 1995).

3.1 Rock Magnetism.

Fundamentally, magnetic signals are held in magnetite because unpaired electron spins in the d orbitals of Fe^{2+} and Fe^{3+} ions have very large exchange energies. The organization of these unpaired spins within the A and B sublattices produces a net magnetization that can become aligned when the mineral cools in the presence of a magnetic field (Tauxe, et al., 2018). If a magnetic mineral is less than 30 nm in diameter, it will not record an ancient direction because ambient temperatures will reset the direction. Grains less than 30 nm in diameter are called superparamagnetic (SP) grains. The magnetic directions held by these nanoparticles flip randomly in response to temperature changes and when measured over a long enough time frame their

magnetization is net zero. However, when exposed to a high external field SP grains can acquire a magnetization. If a mineral is large enough to hold a magnetic signal but not too large it will consist of a single magnetic domain (SD). As the mineral grows the internal energies created by the alignment of electron spins become unstable and the mineral splits into multiple magnetic domains (MD). The grain size of the SD to MD transition is dependent on mineralogy; in the magnetite-titanomagnetite series the grain size of the transition is on the order of micrometers. In MD grains the domain walls can shift in response to an external field so that the domain directions align with the external field. Because SD grains do not contain any domain walls that can be easily reorganized, the direction of the magnetization must flip, which requires much more energy than reorganizing domain walls (Dunlop et al., 1997). The magnetic field strength required to flip the direction of magnetization in a mineral is a property called coercivity. Because of the presence of domain walls, the larger MD grains are more easily remagnetized and have a lower coercivity than SD grains. Drilling induced remanent magnetization (DIRM) is a common overprint which is more likely held by MD grains because they generally have a lower coercivity. The goal of rock magnetism is to identify the magnetic components (SD or MD) that are contributing to the RM so that the demagnetization paths can be correctly interpreted and to isolate the signal held by the SD grains as this is more likely the characteristic remanent magnetization (ChRM) recorded by the rocks at the time of their initial formation.

3.1.1 Rock Magnetism Methods

Nine samples were selected for rock magnetism as representatives of lithology and demagnetization results. These samples are here after referred to as the representative samples. A vibrating sample magnetometer (VSM) was used to measure magnetization in the presence of a magnetic field, producing hysteresis loops (Figure 2), and to obtain induced remanent magnetization (IRM) curves (first column in Figure 3). Saturation magnetization (M_s) is obtained when all magnetic domains are aligned, including those that are not oriented in a favorable direction. M_s is determined from a hysteresis loop at the high field horizontal asymptote. Saturation remanent magnetization (M_r) is a measure of the magnetization when there is no external field. The bulk coercivity (H_c) is the magnetic field needed to flip half of the magnetic domains, producing a net zero magnetization. H_c is determined from the hysteresis loops where the loop crosses the horizontal (applied field) axis. The magnetic field that flips enough domains such that

the net magnetization is zero when the field is removed is the coercivity of remanence (H_{cr}). The H_{cr} was calculated from the mass normalized IRM curves. The ratios of M_s to M_r and H_{cr} to H_c are plotted in Figure 4. Powders and chips of each sample were analyzed, for a total of 18 measurements. See Appendix A for full laboratory procedure and sample masses listed in Table A1.

The IRM curves represent the sum of all magnetic mineral components in the sample. An open source unmixing program, Max-unmix (Maxbauer et al., 2016) is used to determine the coercivity of the individual mineral populations (Figure 3, second column). The Max-unmix software uses a statistical approach to fit multiple curves to an inputted coercivity spectra. Each curve that is added to the model has variables of 1) mean coercivity, which dictates the placement of the curve's peak, 2) dispersion, which controls the width of the curve, 3) the skewness of the distribution, and 4) normalized proportion, which is a measure of how much that curve is contributing to the fit of the data (Figure 3 third column). The observed contribution is the contribution calculated from values below 2.5mT (3 mT in the case of sample 414Ch), whereas the extrapolated contribution is calculated from the full curve, even if it is cut off at the high end of the spectrum, as in the case of component 2 in sample 414Ch (Figure 3 second column). The error analysis is a Monte Carlo calculation with 100 iterations where 95% of the points are drawn from the original data (Figure 3, second column).

Plotting the ratios of M_r/M_s versus H_{cr}/H_c has been used by many as an indication of domain states (Day et al, 1977). Theoretically SD and MD grains should plot in the SD and MD regions of the Day plot (Figure 4). However most samples found in nature fall in the pseudo single domain (PSD) range, which is interpreted as a mixture of SD and MD grains. Dunlop (2002; and references therein) suggests particle size distribution, internal strain and grain shape all effect M_r/M_s and H_{cr}/H_c values. High internal strain, irregular shapes and wide distribution of grain sizes can result in M_r/M_s and H_{cr}/H_c values that plot closer to the SD field.

3.1.2 Rock Magnetism Results

The representative samples selected for this study have H_{cr}/H_c ratios that range widely from 1 to 4, while the M_r/M_s ratios are similar and plot within the PSD range. Samples 414, 828 and 1161 have M_r/M_s ratios between 0.1 and 0.2 and are closer to the MD range than the other samples

that plot along a ratio of 0.25 M_r/M_s . Sample 414 has the lowest H_{cr}/H_c ratio and plots closest to the SD range (Figure 4).

Each IRM curve can be fit by mixing two distinct curves, except for 414Ch which requires three curves to match the data (second column in Figure 3). Samples 414, 828 and 1161 all have a high coercivity component between 1.5 and 1.7 mT as well as a lower coercivity component between 1 and 1.5 mT that is very dispersed and makes up a much smaller portion of the overall magnetization. The rest of the samples have two components that are similar in coercivity and contribution, but one is more dispersed and skewed toward higher coercivity than the other component.

The hysteresis loops from 414, 828 and 1161 are all comparable to an idealized MD hysteresis loop, whereas the rest of the loops are comparable to a mixture of grain sizes (Tauxe et al., 2018). The samples that plot farthest to the right on the Day plot (Figure 4) have hysteresis loops that are most similar to an idealized SP loop.

3.1.3 Rock Magnetism Implications

The similarity in M_r/M_s ratios indicates that each sample has a similar mixture of SD and MD sized grains, apart from samples 414, 828 and 1161 which probably have a larger portion of MD sized grains since they are slightly lower on the Day plot (Figure 4). The spread in the H_{cr}/H_c ratios suggest varied amounts of SP grains within the mixture of SD and MD grains. Samples that plot farthest to the right on the Day plot (Figure 4) likely contain higher proportions of SP grains. The hysteresis loops of these samples also suggest high amounts of SP grains as their shapes are closest to an idealized SP loop.

Unmixed IRM curves suggest that there are two prominent magnetic components in all samples and three in sample 414Ch. The dispersed component in samples 414, 828 and 1161 could be the manifestation of a higher amount of MD grains in a mixture with SD+SP grains. The skewed component in the rest of the samples could be the result of a higher amount of SD grains within the mixture or could indicate a mixture of different mineral phases (pyrrhotite or Ti-hematite).

Analysis of the representative samples has shown that all samples have some component of SD grains with coercivities between ~25-60mT, as well as an MD component with much lower coercivities. Rock magnetic properties do not vary much between lithology.

3.2 Paleomagnetic Directions

3.2.1 Demagnetization Method

The fractured core pieces were reassembled into “runs” using the fit of individual pieces or through-going rock fabric, and a false north reference mark (N’) was made along the length of each section (Figure 5). Each run is separated from the next where the core could not be fitted back together. This disconnect occurs where the core is so heavily fractured as to be rubble, where there are pieces missing, where the core has been cut for sampling without being marked, or where the core pieces were deformed because of drilling complications. It is important to note that rubble zones occur along the brecciated tops of lava flows and are likely important permeable planes within the substrate. Runs that were selected for this study are listed in Table 1. These runs were chosen because they contain the highest density of cross cutting veins and because they contain the most reliable paleomagnetic directions. The assumption is made that veins within the intact sections of core have orientations that approximate those in the rubble zones. Sampling for RM analysis was restricted to igneous units; basalts, andesite, and tuffs that were relatively free of veining and at least two feet away from intense hydrothermal alteration. This alteration often occurs along contacts between lithologies or the brecciated tops of flows. Sample ID numbers are grouped in a hierarchy by locality, site, sample, and specimen. Each core is a locality (e.g., TG-4), each run in the core is a site, each flow unit in that run is a sample, and each individual paleomagnetic cylinder drilled from the core is a specimen with the naming scheme: (footage)-(piece number in the box)(specimen in sample). All analyses were done in the Pacific Northwest Paleomagnetic Laboratory following standard demagnetization procedures (see appendix A. for complete laboratory procedures).

Flow units were defined by changes in lithology or chilled margins separating flows of the same lithology. Six specimens were drilled in each run that hosted an appropriate lithology. If the run had multiple flows appropriate for sampling, three specimens were taken from each additional flow. Specimens were drilled relative to the false north mark through the center of the core, so that the positive x direction on each specimen is parallel to N’ and in the up-core direction as in Figure 5, see Figure 6 for run lengths and sample locations. The cylinder samples are taken from the center of the core to avoid drill induced remagnetization that could have affected the outside of the core (Pinto and McWilliams, 1990).

Half of the specimens from the samples with six specimens and all the specimens from the additional samples were demagnetized with increasing strength of an alternating field in the D-Tech 2000 AF (de)magnetizer. The other half of the six specimen samples were thermally demagnetized. Specimens with high magnetic moments were measured on the spinner magnetometer and the rest were measured on the 3-axis 2-G Enterprises model 755 cryogenic magnetometer between each demagnetizing step. Principal Component Analysis (PCA) (Kirschvink, 1980) was used to define paleomagnetic directions from demagnetization steps within the PuffinPlot (Lurcock and Wilson, 2012) software. Fisher statistics (Fisher, 1953) were used to calculate the mean declination and inclination of groups of specimens. Finally, selected directions with negative inclinations were converted to the lower hemisphere so that the reorientation calculations were consistent across all sites, effectively adding 180° to the declination.

The original directions and the inverted directions used for reorientation are listed in Table 2. The directions selected to reorient the core had to pass three standards. First, directions from individual specimens should be well-defined, with at least four demagnetization steps defining the characteristic remanence, with a MAD angle of $<6^\circ$ for the PCA fit. Secondly, directions had to have a normal or reverse inclination like that which would be expected at Akutan: between 60° and 85° . And thirdly, directions from sets of specimens from a flow unit or intact core run should be consistent, with a k value >15 indicating a tightly clustered data set. Only 6.7% of the specimens collected were used in the final core reorientation.

Commonly in paleomagnetic studies a virtual geomagnetic pole (VGP) is calculated from sets of samples or specimens that represent a single, or geologically short, interval of time. If VGP's are averaged over $\sim 10,000$ years they approximate a geocentric axial dipole (GAD) field, which provides the best-defined geomagnetic field reference direction for a specific geographic location because the location of the magnetic north pole corresponds to the geographic spin axis for this field geometry. As a result, it is considered best practice to sample at least 10,000 years of the rock record to average out this paleosecular variation. For volcanic rocks, each cooling unit will only record the geomagnetic field over a short duration of time. This study lacks independent data with which to define cooling units so rely of flow units. However, because of the limited number of flows within intact runs of the core, it must be assumed that there is not enough time sampled to average out paleosecular variation. Paleosecular variation models typically have a

(VGP) dispersion of about 30° from the GAD field (Johnson and Constable, 1996). Stone and Layer (2006) showed that the paleosecular directions from the Aleutian Islands for 0-2 Ma have a much smaller directional dispersion than what is predicted by current paleosecular variation models. The dispersion measured from flows across the Aleutians have a VGP dispersion of 6.43° from the GAD field, and when data from western Canada is added the VGP dispersion is 12.07°. Therefore, the reoriented structural measurements used in this study have a reorientation error of at least ±6.43° and up to ±30° in the strike direction. Also, because Akutan is at a high latitude the inclination angle is steep and therefore there is greater inherent error in the declination direction of any magnetic signal compared to a similar sample from lower latitudes.

The amount of rotation (R) and compounded error (ΔR) for each site is calculated as the difference between the declination of the mean direction observed (D_o) in each site to the declination of the expected magnetic direction (D_x) at Akutan by,

$$R = D_o - D_x \quad \text{Eq.1}$$

and,

$$\Delta R = 0.8\sqrt{\Delta D_o^2 + \Delta D_x^2} \quad \text{Eq.2}$$

(Demarest, 1983). In this case the declination of the expected direction is D_x= 0, or directly north. The confidence limit on the expected declination (ΔD_x) is calculated by

$$\Delta D_x = \sin^{-1} \left(\frac{\sin A_{95}}{\sin p} \right) \quad \text{Eq.3}$$

where A₉₅ is the 95% confidence limit on the mean VGP and p is the magnetic colatitude, the angle between the site location to the equator. Here A₉₅=13° as in Stone and Layer (2006) and ΔD_x = 22.6° as calculated from Eq.3.

3.2.2 Demagnetization Results

Robust sampling insured that usable paleomagnetic data was acquired, however the side effect of this choice is that much of the paleomagnetic data remains unused. In some cases, a site only contains one place appropriate for sampling (e.g. Figure 6. 271-274ft.), even if multiple flows exist in the site. Many of the sites defined are too small (Figure 6) or do not contain enough structures to justify creating an unrolled image (as discussed in section 4.1). Typically, the first

component of the paleomagnetic directions throughout each run varies between samples and sometimes between specimens within the sample. This was anticipated given the possibility of a DIRM overprint. The second or third component within each specimen are typically consistent over multiple specimens and samples. While the directions are very well defined most do not fall within the required inclination angle. Results are presented generally by each lithology, for sites not selected for reorientation (totaling 93.3% of the demagnetization data), and more specifically by site and sample for sites that were selected for reorientation. Results from selected sites are presented in Table 1 (see appendix B for full list of site, sample and specimen data).

Specimens that were drilled in the tuff lithology have two components, the first-removed component is usually very small and poorly resolved and the second is well defined (Figure 7). A few of the specimens treated with alternating field demagnetization have components that are overlapping causing the demagnetization paths to be curved. The alternating field demagnetization curves are straight to slightly concave up and usually reach <10% of NRM by either 20 mT or ~60 mT steps (Figure 7.A). Thermal demagnetization curves reach < 10% magnetization by 600 °C with a sharp decline between the 120 °C and 200 °C heating steps (Figure 7.C) and the 500 °C and 600 °C heating steps. Some do not have a significant drop in magnetization between 120 °C and 200 °C (Figure 7.B).

Specimens drilled from andesite usually have a scrambled (Figure 8.A) or horizontal (Figure 8.B) first component and a highly inclined and well defined second component. The thermal demagnetization curves reach <10% NRM by the 600 °C heating step with a sharp decline between the 500 °C and 600 °C heating steps (Figure 8.A). The AF demagnetization curves are usually straight to slightly concave up and reach <10% NRM by either the 60 mT or rarely the 100 mT step (Figure 8.B). Some of the thermally demagnetized specimens have only one component. Demagnetization curves for the single component andesite specimens have a steady rate of decline and reach <10 % NRM by the 400 °C heating step (Figure 8.C). The AF demagnetization curves from the same sample sites have a steady rate of decline that reaches <10% of NRM by the 35-40mT steps (Figure 8.D).

Many of the specimens drilled from basalt have two components. The first component is vertical with a negative inclination, and the second is usually steeply dipping with a positive inclination. The first component is defined by the 0-10mT AF steps (Figure 9.A) and the 0-400 °C

thermal steps (Figure 9.B). The second component is defined by the 15-70mT steps and the 500-600 °C thermal steps. Both the AF and the thermal demagnetization curves increase over the steps that define the first component and decrease over the steps that define the second component. The AF demagnetization curve reaches <10% NRM by the 60-70mT steps and the thermal demagnetization curve by the 600 °C step. Some of the basalt specimens have a single component that is defined by the 0-35mT (sometimes as low as the 0-15mT step) and the 120-400 °C thermal steps. The thermal demagnetization curves have a steady decrease throughout all temperatures and reach <10% NRM by the 400 °C step (as in Figure 8.C). The alternating field demagnetization curves decrease sharply in the first few steps and then shallowly, creating a distinctive 'L' shape, reaching <10% NRM by the 15 to 35mT step (as in Figures 8.D and 7.B).

The 588.5-595.5 ft. (179.4-181.5 m) site has two units which were acceptable for sampling, an andesite and a basalt. The andesite flow unit is ~ 1 m thick (Figure 6.) and the basalt is ~12.8 m thick. The specimens collected from the basalt are within a meter of the top flow margin. Every specimen revealed a well-defined magnetic direction with two components. The first component is interpreted to be an overprint from drilling of the TG wells because it is near vertical and the declination is varied. The second components were added to the site mean. Specimens 589-2B, C, F, and 594-2B had second components with inclinations steeper than 85 ° and so were removed from the site mean calculation (Figure 10).

The 831-841 ft. (253.3-256.3 m) site contains two flow units, a ~3.6m thick basalt and a ~14.3m thick andesite (Figure 6), however only the basalt was appropriate for sampling. Specimens were collected within and 10cm of the bottom flow margin. All specimens had magnetic directions with two components. The first component in each specimen is vertical and is interpreted as a DIRM. The second component in each specimen has a negative inclination and was added to the site mean (Figure 10).

The 942-983 ft. (287.1-299.6 m) site contains eight units, five of which were sampled (Figure 6). Samples 947-10, 955-9, and 957-15 are all from flow units that are ~1-3m thick (Figure 6). The inclination from sample 947-10 are below 65°, the declinations in each specimen from sample 955-9 are alternating ~180°, which is interpreted as a sampling overprint (see Appendix A), the magnetic directions from sample 957-15 have vertical first components and inconsistent second components, which is interpreted as a DIRM (Table 1); all were removed from the site

mean calculation. The first component in sample 965-11, a 2.4m thick andesite, aligns well with the second component, in sample 971-2 (Figure 11), a 4.5m thick basalt. The 965-11 sample was collected within 10cm of the bottom margin of the flow, directly above the basalt (Figure 6).

The 1022.5-1030 ft. (311.7-313.9 m) site contains one basalt flow that is ~9m thick. The first component in all specimens is near vertical with a varied declination and the second component is steeply dipping with a consistent declination (Table 1). The first components are interpreted to be a DIRM and the second components were added to the site mean. The second components in specimens 1024-2A, B and F have inclination that are steeper than our cutoff and so were removed from the site mean.

In the 1030-1066 ft. (313.9-324.9 m) site there are seven flow units, five of which were sampled (Figure 6). The thickness of these flow units ranges from 1-9m and all samples were collected within 10cm of a flow margin. Two consistent directions that pass our standard for reorientation are present in the specimens from the 1030-1066 ft. (313.9-324.9 m) site. The consistent direction between samples 1041-16 and 1042-1 has a reverse inclination and is defined by the 500-600°C temperature steps. These samples also have a first or second component with normal polarity that are consistent in inclination but vary in declination. The directions from sample 1053-4 and 1065-16 both have a normal inclination that matches the modern inclination at Akutan, and a consistent declination. Both consistent directions could be a ChRM and used for reorientation.

3.2.3 Interpretation of Paleomagnetic Directions

The temperature range that defines the components used to reorient sites 588.5-595.5 ft. (179.4-181.5 m), 831-841 ft. (253.3-256.3 m), and 1022.5-1030 ft. (311.7-313.9 m) is 500-600 °C and indicates that magnetite is the mineral holding the magnetic signal. I propose that the basalt at 965 ft. depth, in the 942-983 ft. (287.1-299.6 m) site intruded into the andesite unit above it and the heat caused a thermal overprint in the andesite flow (sample 965-11). Therefore, the second component in the basalt is interpreted to be the ChRM and the first component in the andesite is interpreted to be a thermal overprint caused by the intrusion. This direction was used to reorient the 942-983 ft. (287.1-299.6 m) site (Table 2). The two consistent directions in the 1030-1066 ft. (313.9-324.9 m) site could be a ChRM and used to reorient the site. However, since the direction from samples 1041-16 and 1042-1 has a reverse inclination it must be an ancient direction, whereas

the direction from samples 1053-4 and 1065-16 is normal and might be a DIRM since the first and second components are almost indistinguishable. Therefore, the reverse polarity direction in the 1030-1066 ft. (313.9-324.9 m) site was used to reorient that section of the core.

The rotational error on the declination of site means ranges from $\pm 9.9^\circ$ to $\pm 22.2^\circ$ (Table 2, Figure 10). This error is passed on to the strike of any structural data within the site. While each site has a slightly different strike error every strike within a site has the same magnitude of error. In other words, a cluster of data from within a single site has an error associated with it, but individual structural measurements within a site do not have different strike errors.

4. Structural Investigation

Constraining permeability is the most challenging aspect of geothermal exploration and development (Coolbaugh et al., 2015). Hinz et al. (2016) has shown that the most productive geothermal systems worldwide are associated with structural environments that are complex, with intersecting fault zones, and tectonic environments with any component of extension. Understanding the structure of hydrothermal pathways and the stress states that widen them is a goal that can be met by inspecting the record of past rupturing events. Details of rupturing events can be determined by hydrothermal mineralogy. For example, when hydrothermal fluids heat up, as they move closer to the reservoir, the solubility of calcite decreases, causing mineral growth but quartz becomes more soluble (Elders et al., 1981). For this reason, the inflow pathways are commonly identified by the presence of calcite. Mineralogy in upflow and outflow pathways, where temperature decreases with distance, is more commonly dominated by quartz and chlorite, with only minor calcite (Elders et al., 1981). Boiling during fluid ascent can cause dramatic changes in the environment of hydrothermal systems and because of this multiple mineral species can crystalize simultaneously (Drummond and Ohmoto, 1985). Veins that are laminated with calcite \pm chlorite \pm quartz \pm hematite could be the result of multiple rupturing events or the result of progressively changing fluid chemistry and or temperature causing systematic mineralization. Sections of the TG-4 drill core were reoriented using the declination of paleomagnetic site means and the measured structural and mineralogic features were used to investigate the link between seismic events on Akutan and the productivity of the HSBV hydrothermal system.

4.1 Core Analysis

4.1.1 Core Analysis Methods

Core sections were chosen for structural analysis if they 1) encompassed usable paleomagnetic specimens, and 2) contained a high density of veins and cross-cutting structures. Each selected core run was photographed with a Nikon COOLPIX B500 digital camera. The core segments were placed on a rack with a green screen background that was later masked out of the images. Model building followed the standard Agisoft workflow, and a cylindrical projection was used to create an “unrolled” image of the outside of the core (Figure 5; see Appendix A for full workflow). The open source software ImageJ was used to generate a list of pixel coordinates from these images from which the strike, dip, and depth of fractures, veins, contacts and matrix permeability were calculated in an excel spread sheet (see appendix B for structural data). The mineral fill was identified, and rake of slickenlines was measured by hand. Slickenlines were assigned low- or high-confidence levels based on the quality and prominence of directional movement indicators. Cross cutting relationships were noted when present. A vein was deemed “cross cutting” if there were subtle offsets or if mineralization clearly overprinted the other structures. If a fracture or vein was offset by more than a few millimeters it was not directly measured, as the offset h measurement would not produce accurate dip data. Instead a vein of similar orientation within the run was used as a placeholder for the offset structure.

A flat structural feature in the core appears as a perfect sinusoidal curve in the core log images (Figure 5). To calculate the strike and dip of structures the pixel coordinates of the peak (T) and troughs (B) of the sine curve as well as the coordinates of the N' line were extracted from the two-dimensional core log image with ImageJ and used as inputs in an excel sheet. To convert the measurements from pixels to meters the pixel width of the image, and the pixel length of a scale parallel to the length of the core were extracted with ImageJ and used as inputs in the excel sheet. The scale parallel to the length of the core was used to calculate the depth of each feature at T. The difference between the T and B of the curve (labeled (h) in Figure 5) is used with the diameter of the core (d) to calculate the dip of the structure by $dip = \tan^{-1}\left(\frac{h}{d}\right)$. For the strike measurement to be in the right hand rule the pixel coordinates of the inflection point where the curve increases to the right is used as the strike. The x and y coordinates of the inflection point are calculated as the median value of the x and y coordinates of T and B. The pixel distance between

the N' line and the x value of the strike point is the azimuthal strike in the N' coordinate system. The pixel strike is converted to degrees using the conversion factor of $\left(\frac{\text{pixel width}}{360 \text{ deg}}\right)$. The declination of the site mean is then used to convert the strike measurements from the N' coordinate system to true geographic north, albeit with error inherited from the uncertainty of the paleomagnetic directions (see section 3.2.1). These calculations were done in an excel spread sheet.

Irregular structural planes introduce error into these calculations because the calculations are based on an assumed perfect sine curve. Additionally, if the 3-dimensional model is misshapen significantly because of poorly aligned photographs the 2-dimensional projection will be distorted, and the structural trace will not be a perfect sine curve even if the structural is perfectly flat in hand sample. It is then important to collect enough overlapping photographs from which to make the models as accurate as possible. A randomly selected subset of orientation data was also measured by hand with a Brunton compass and compared to the calculated orientations (Figure 12). The amount of error on the calculated orientations is comparable to that of measurements made by hand as both are done on a small portion of a much larger plane. Therefore, as with structural measurements made by hand in the field, I rely on a large data set to define general orientations of structural features which can be related to island scale trends mapped on the surface.

4.1.2 Core Analysis Results

A total of 530 planar features were measured and reoriented using the declination of the site mean (Figure 13). Note that the clusters of data in the unoriented core (Figure 13a) result from a large portion of the data being present in a few long core runs. Of the data presented in Figure 13b, 477 are mineralized veins and 53 are un-mineralized structures. The orientations of un-mineralized structures (i.e. fractures; Figure 14.A), have dips that are generally within 30° of horizontal and average around horizontal with a random distribution of strikes (Figure 14.A). Many of these unmineralized fractures have jagged faces and or terminate where truncated by mineralize veins. Because many of the fracture are consistent with drilling-induced and handling-induced stresses, and because unmineralized fractures contain no information about the history of the hydrothermal fluid flow, these have been removed from the data set. These 53 fractures make up only 10% of the data set, the other 90% of the structural data is useful to our study. As a result, all the subsequently discussed veins sets are subsets of the veins presented in Figure 14.B. Mineralized veins have strikes in a wide range of directions (Figure 14.B). However, there is a

prominent NW striking, NE dipping cluster as well as a more dispersed SE striking, SW dipping cluster.

Vein width, (distinct from aperture, discussed below), is here defined as the width of the mineralized zone. Vein widths vary though most are less than 1mm thick (Figure 14.C). Although veins <1mm wide strike in all directions, the dominant orientation is to the NW and dip ~60° to the NE. Veins that are 2-4mm, 5-9mm and >10mm wide are present throughout the bottom three runs and are most abundant in the 313.9 – 324.9 m. range (Figure 14.D, 14.E and 14.F, respectively). Veins of all widths are predominantly striking to the NW and dipping to the NE, with a smaller number of veins striking to the SE and dipping to the SW. Overall the orientation of veins becomes more ordered with depth, with the widest veins present at the greatest depths.

Polymineralic veins are abundant, and many contain crack-seal textures observed in thin section (Figure 15). Monomineralic veins are predominantly calcite filled (Figure 15, 4-83-542 upper left) and are more often thin, hairline veins. Calcite filled veins dominate the core (Figure 16.A) and most are NW striking and dip to the NE, whereas the orientation of chlorite filled veins (Figure 16.B) are more dispersed. Purely chlorite-filled veins are concentrated in the upper portions of the core (0 - 317 m) whereas purely calcite filled veins are present throughout (Figure 16.A). Quartz is present in only 13 out of 477 veins and is always accompanied by calcite and or chlorite (Figure 16.C). Hematite and zeolites such as lawsonite and chabazite are present as well but only as accessory minerals in polymineralic veins (Figure 15).

Veins that have open apertures are concentrated at specific depths (~180 m, between 289-292 m, ~313 m, and ~322 m depth) and have a range of orientations (Figure 16.D). Most apertures are less than 1mm although the partially mineralized veins below 322 m depth have apertures up to 2cm wide as well as bladed calcite with argillic alteration and intense hairline veining extending up to 8cm into the wall rock.

Cross-cutting relationships between veins are also present in the core. The orientation of veins that are cross-cutting (Figure 16.E) and those that are being cross-cut (Figure 16.F) are very similar. Both conditions have clusters of orientations with strikes to the NW and S with dips to the NE and W, respectively. Because of these similarities fault sets based on orientation cannot be separated temporally. However, vug and vein fillings viewed in thin section show that calcite and zeolites are always the last to form (Figure 15).

Throughout the ~31 m of reoriented core there are 86 mineralized and two unmineralized faces with slickenlines. The sense of slip indicated by the slickenlines was not always clear, so each measurement was given a confidence ranking from 0-5, with 5 assigned to measurements with a clear sense of slip and 0 an ambiguous sense of slip. Of these, 58 are high level confidence (Figure 17.A), and the remaining 30 are low level confidence. Purely calcite filled veins with slickenlines of high confidence numbered 15 (Figure 17.E), and 10 purely chlorite filled veins with slickenlines of high confidence are present (Figure 17.F). Veins with slickenlines, hereafter referred to as shear veins, have three primary orientations, WNW dipping, NE and SW dipping, and a small number of E-W striking planes (Figure 17.A). The SW dipping shear veins have slickenlines showing oblique normal movement down to the NW, W, and SW. These NW striking, SW dipping shear veins are filled with calcite after chlorite (Figure 17.B). The NW striking, NE dipping set have slickenlines that show oblique normal movement to the NNE and are primarily filled with pure calcite (Figure 17.C, E). The NNE and E-W striking shear veins have primarily sinistral strike slip movement indicators and are polymineralic, hosting chlorite \pm other minerals (Figure 17.D) or monomineralic, hosting only chlorite (Figure 17.F). Three of the shear veins with laminated mineral growth have slickenlines on multiple mineral lamination faces within the same vein. The rake of these slickenlines show two distinct movement indicators for the same structural surface (Figure 18). The cross cutting slickenlines show oblique normal-sinistral movement whereas the cross-cut slickenlines show reverse movement on two planes and normal movement on the other.

4.1.3 Implications of Reoriented Structures and Minerology

Vein width, mineralogy, and style of mineralization in part reveal the rupturing history of the geothermal system in HSBV. Vein width can be interpreted as a large aperture being slowly filled in, indicating high permeability; or a small, repeatedly opened aperture, indicating episodic fluid flow. Polymineralic veins could be the result of mineralization during boiling or of repeated rupturing and episodic fluid flow. Multiple orientations of slickenlines on separate mineral laminations within a single vein, and the abundance of crack-seal textures observed in thin section (Figure 15) are evidence of multiple rupturing events rather than systemic mineralization caused by boiling. Veins with a monomineralic fill, and veins that are less than 1mm thick are interpreted to show single fluid flow events. It is possible that long lived continuous fluid flow could deposit a single mineral type if the source fluid had a static chemistry but given the abundance of polymineralic

veins in the core, the monomineralic, thinner veins are more likely to be the result of a single, short-lived fluid flow event. Veins wider than 1 mm (Figure 14.D-F) are interpreted to indicate sustained or multiple fluid flow events. Because cross cutting vein sets could not be separated temporally, shear veins were grouped based on mineralogy (Figure 17) with the reasoning that veins of similar mineralogy likely formed from a similar fluid source and stress field. Chlorite and calcite were chosen as the mineral delimitators because these are the primary geothermal minerals in the core and form in different hydrothermal environments. As discussed in Section 4, the presence of calcite in a vein indicates that that structural feature acted as an inflow path to the reservoir, whereas the presence of chlorite is more indicative of hydrothermal outflow. Fractures are interpreted as non-fluid hosting and therefore are not relevant to this study.

4.2 Paleostress Inversion

The determination of paleostresses or in situ stresses from fault slip data has been the goal of many researchers. One of the main failings of many studies is the use of heterogeneous fault slip data for principal stress inversions (Sperner and Zweigel, 2010). Heterogeneous fault slip data is the result of multiple stress states and must be separated into temporal subsets based on geological evidence or geographical regions of homogenous strain (Simón, 2018). Temporal delimitation is not possible for this study because, as discussed in section 4.1.2, cross cutting relations between fault sets based on orientation are inconclusive (Figure 16.E, F).

4.2.1 Paleostress Inversion Methods

The multiple inverse method (MIM) (Yamaji, 2000) is a statistical algorithm based on the inverse method (Angelier, 1984) that can effectively test whether a set of fault slip data resulted from homogenous or heterogeneous stresses. The MIM calculates a stress tensor which minimizes the angular difference between observed and theoretical slip directions on a set of fault planes. The stress tensor is described by three directional components as well as the Lode number (μ_L) (Lode, 1925), which describes the shape of the stress ellipsoid where,

$$\mu_L = \frac{2\sigma_2 - \sigma_1 - \sigma_3}{\sigma_1 - \sigma_3} \quad \text{Eq. 4}$$

given that $\sigma_1 \geq \sigma_2 \geq \sigma_3$. The Lode number ranges from -1 to +1 where the end member values represent uniaxial compression and uniaxial tension respectively and intermediate values indicate triaxial strain. Although Angelier's inverse method uses Bishop's parameter (Φ) to describe the

shape of a stress ellipsoid, the Lode number is more desirable for the MIM algorithm because end members have the same absolute value. The Bishops parameter is related to the Lode number by

$$\mu_L = 2\Phi - 1 \quad \text{Eq. 5}$$

and varies from 0 to 1 where the end members represent uniaxial compression and uniaxial tension, respectively. It should be noted that the most recent version of the MIM software uses Φ to describe the relationships between principal stresses. The three directional components and Φ are plotted in a four-dimensional parameter space to define a stress state. The best fit to the input data is indicated by a cluster of similar σ_1 and σ_3 directions with similar Φ values. If multiple clusters (i.e. multiple solutions) are observed, the data is said to be heterogeneous, resulting from multiple or changing stress states. Simón (2018) has suggested using at least 10 but preferably 15 faults with directional data in any stress inversion. The MIM program also requires at least 15 data points to produce an interpretable result.

As discussed above (Section 4.1.2) only 15 purely calcite filled and 10 purely chlorite filled shear veins with high confidence slickenfibers are present. Shear veins with chlorite and other minerals, primarily calcite, were added to the chlorite data set to obtain a large enough data set for the MIM to function. Likewise, polymineralic shear veins with calcite \pm hematite \pm quartz, but not chlorite, were added to the calcite data set. Finally, the MIM calculation was run on shear veins with chlorite and calcite fill. Shear veins with multiple slickenline orientations were excluded from the final MIM calculation because the method only uses one rake measurement for each surface and because the crosscutting relations of the slickenlines is low confidence. However, the MIM was run with the ‘older’ and ‘younger’ generation of slickenlines for the sake of comparison.

The uncertainty in the direction of principal stress orientations results from the uncertainty of each fault plane in the data set. The error contributed by each shear vein within a run is the same, however each run contributes a unique error (inherited from paleomagnetic directions, see section 3.2). To calculate the directional error on each principal stress orientation a weighted average of the site errors was taken, with the weight on each error being the percentage of shear veins that come from the site with that error. The error in the plunge of each principal stress orientation can be estimated by the vertical spread in the solution clusters and is therefore independent of the inherited paleomagnetic errors.

4.2.2 Paleostress Inversion Results

Results of the MIM analysis on all 55 high confidence shear veins show heterogeneous strain because there are multiple clusters (i.e. multiple solutions) produced by the calculation. Broadly there are four orientations of principal stress that fit the data, and each cluster of solutions fits a different combination of fault sets (Table 3, Figure 19, Figure 20).

The first orientation group has a horizontal σ_1 oriented NNW-SSE, with a subhorizontal σ_3 oriented ENE-WSW and a Φ value of 0.4. This first group of solutions is visible when all 55 high-confidence data points are included (Figure 20) and when all shear veins with chlorite are included (Figure 21), but the cluster of solutions is much larger when shear veins hosting chl + cal \pm hem \pm qtz are considered (Figure 22). Furthermore, Φ value drops to 0.2 when pure calcite filled shear veins are removed (Figure 21). The plunge of σ_3 ranges from horizontal WSW to $\sim 25^\circ$ to the ENE. Evaluating the misfits at each end of this range shows that similar, although not identical combinations of faults are activated under each σ_3 endmember. The shear veins that best fit this stress state have steep dips and slickenlines that indicate oblique normal or strike-slip movement.

The second orientation has a σ_1 direction with an azimuth orientation in the SW and a steep plunge of about 50° (Figure 19). The corresponding σ_3 direction is the same as the ENE endmember in the first group; trending ENE with a $\sim 25^\circ$ plunge. When all 55 shear veins with high confidence slickenlines are considered there are two distinct values of Φ in this third group; 0.1 and 0.6 meaning that the stress ellipse is either strongly oblate or triaxial (Figure 20). When pure calcite shear veins are removed from the data set the Φ values are 0.2 and 0.8 (Figure 21), and when calcite + chlorite shear veins are considered there are three values of Φ ; 0.2, 0.6, and 0.8 (Figure 22). The $\Phi=0.8$ cluster is much smaller in the calcite + chlorite data set (Figure 22) than in the chlorite – calcite data set (Figure 21).

The third orientation of stress states has a σ_3 direction with an azimuth direction in the NE and a $\sim 30^\circ$ plunge (Figure 19). The corresponding σ_1 is a great circle perpendicular to σ_3 because the Φ value is one, meaning that $\sigma_1=\sigma_2$ and that the stress ellipse is elongated in the direction of σ_3 .

The fourth group of stress states that fit the data has more variation in the orientation of the principal axes and the Φ value. The σ_1 axes in the fourth group has an azimuth orientation in the NW and a plunge that varies from $20-60^\circ$ (Figure 19). This fourth orientation is only present when

mono and polymineralic shear veins hosting calcite but not chlorite are considered (Figure 23) and when all 55 high-confidence data points are considered (Figure 20). When the data set is considered as a whole, there are four values of Φ (0.2, 0.3, 0.5, and 0.8), this means that stress ellipses with very different shapes have roughly the same orientation of principal stress axes (Figure 20). The main result for calcite – chlorite hosting shear veins is that there are distinct clusters of solutions with Φ values (0.0, 0.1, 0.2, 0.3, 0.4, 0.5, and 0.6) that range from uniaxial compression and to triaxial strain (Figure 23). Furthermore, the first two groups of orientations discussed are not present at all when mono and polymineralic calcite – chlorite shear veins are considered (Figure 23); the third group ($\Phi = 1.0$) is present but the cluster of solutions is small.

Even though the three shear veins with multiple slickenlines were low-confidence the MIM was run separately with the ‘older’ and ‘younger’ slickenlines added to the full high-confidence dataset. When the ‘younger’ slickenlines were considered the fourth orientation group is more pronounced and the maximum stress is closer to horizontal. When the ‘older’ slickenline are considered the second and third orientations are more tightly clustered however the group four orientations are more scattered.

The rotational error of each site ranges from 9.9° to 22.2°, and while shear veins from each site are present in the dataset, the majority come from the longest sites 287.1 - 299.6 m (942-983 ft) and 313.9 - 324.9 m (1030-1066 ft). Therefore, the weighted directional error on each principal stress orientation relies heavily on the rotational error from these sites ($\pm 22.2^\circ$ and $\pm 21.3^\circ$, respectively). Results are presented in Table 3.

4.2.3 Interpretation of Stress States

The data presented reveals much about the structure of the geothermal system at Akutan. Multiple solutions for paleostress calculations show a complex deformation history with multiple principal stress directions and, I propose, changing magnitudes of stress. The chlorite-bearing shear veins that fit orientation groups one and two are interpreted to result from a stress state with a constant σ_3 orientation and a σ_1 that alternates from horizontal to steeply dipping. The calcite hosting shear veins that fit orientation groups three and four are interpreted to have resulted from changes in the relative magnitudes of sigmas 1, 2, and 3.

Results of the MIM analysis on mono and polymineralic calcite filled shear veins show heterogeneous Φ and homogenous principal stress directions with σ_1 in the NW and σ_3 in the SW

(Figure 23). The range in Φ values with similar orientations of σ_1 and σ_3 is interpreted as the intermediate stress changing substantially from very close to σ_1 to very close to σ_3 . The σ_2 direction corresponding to the data presented in Figure 23 is oriented at approximately 125 degrees, with a plunge of approximately 50 degrees.

5. Discussion and Summary

There has been a documented increase in the heat output at the hydrothermal field in Hot Springs Bay valley on Akutan, Alaska (Bergfeld et al., 2014). Approximately 31 meters of drill core over a 145 m range within the total 390 meters of core from the TG-4 well drilled in 2010, has been reassembled and reoriented using remanent magnetization as an indication of geographic north. Two-dimensional core logs were created from three-dimensional digital reconstructions made with structure from motion software. The orientation of structural features was measured from these two-dimensional core logs. This novel application of the Agisoft PhotoScan software could be used for core log creation, as in this study, or ground truthing down-hole geophysical logs.

I hypothesized that if the 1996 seismic swarm caused an increase in the heat outflow of the hydrothermal system at HSBV by rupturing the NW trending fault system, as Bergfeld et al. (2014) suggested, then the NW trending set of veins would be the youngest observed in the core. This hypothesis proved to be too simplistic as cross cutting relations (Figure 16) and MIM analysis results (Figures 17-21) reveal a complicated network of structural features beneath HSBV. In particular, NW and NNE trending vein sets appear to be coeval and have likely ruptured repeatedly over the lifetime of the hydrothermal system, such as in the 1996 event. This is a small window into the intricacies of this system, yet the results presented above hold important information about recharge pathways that sustain the system.

The mineralogy of NW striking veins in well TG-4 is predominantly pure calcite, however there are calcite veins with laminations of chlorite and trace amounts of quartz present as well. The presence of pure calcite veins indicate that the NW trending structures act locally as inflow pathways because the solubility of calcite decreases with increasing temperatures (Section 4). The wide NW trending veins with drusy calcite and apertures up to 2cm below 314 m depth are strong

evidence of this. Well TG-4 is outside of the main upflow region (Stelling et al., 2015) therefore it is reasonable to find mineralogy that is typically associated with the inflow.

It is reasonable to assume two sources of stress on Akutan: tectonic and volcanic. Tectonic forces produced by the oblique subduction of the of the Pacific plate under the North American plate cause differential strain accumulation in the Aleutians that is manifested as partial block rotation and arc parallel extension (ENE/WSW in the eastern Aleutians) (Ave Lallemand and Oldow, 2000). On a more local scale, volcanic fluctuations cause dynamic compressional and tensional stresses to periodically overwhelm the background tectonic stresses (Syracuse et al., 2015; DeGrandpre et al., 2017). Dike emplacement events occur repeatedly on Akutan (Byers and Barth, 1953) and cause localized subsidence or inflation, as was documented after the 1996 seismic swarm (Lu et al., 2005). Lu et al. (2005) modeled changes in ground surface morphology as the emplacement of a dike under the NW flank of the volcano parallel to NW striking ground cracks that were observed after the 1996 seismic event.

Separating the MIM datasets by mineralogy reveals that chlorite filled shear veins are the results of heterogeneous stress, including distinct stress states with horizontal maximum and minimum stresses causing strike slip movement as well as stress states with steeply dipping maximum stress causing oblique normal faulting (Figure 21). I propose that the chlorite filled structures are the result of background tectonic stresses. The arc-parallel ENE/WSW orientation of σ_3 in the chlorite and calcite data sets is consistent with the findings of Ave Lallemand and Oldow (2000), who documented arc-parallel extension. Because both steep and horizontal maximum stress directions fit the chlorite data set it might be that block rotation is intermittent, punctuated by periods of normal faulting. Substantial block rotation would pose an added error to paleomagnetic directions used for the reorientation of the core. However, since paleomagnetic sampling was only done at one locality (TG-4) there is no way of detecting the rotation.

Calcite filled shear veins also result from heterogeneous stress however the orientation of the maximum and minimum stresses remains approximately constant while Φ values vary (Figure 23); this is interpreted as a dynamic stress state. I propose that the calcite filled structures are the result of deformation caused by volcanic activity; specifically, that dike injection caused the magnitude of σ_2 in the group 3 paleostress orientation to increase so that $\sigma_2 \approx \sigma_1$ resulting in the $\Phi = 1.0$ paleostress. The $\Phi = 1.0$ paleostress fits the same fault orientations in the core (Figure

20) that were mapped on the surface (Figure 24) (Stelling et al., 2015). The group 3 paleostress orientation could represent the initial rupturing in a dike emplacement event. Although there is no way to link these exact shear veins to the 1996 event, the dynamic stress state recorded as the group 3 paleostress fits with our expectations for a stress state influenced by volcanic forces. The changing Φ values in the group 4 paleostress fit the NE and SW dipping oblique normal faults (Figure 20, 23), primarily filled with calcite. This could represent subsidence or settling of the hydrothermal system, such as that which was documented in the years following the 1996 seismic swarm (Lu et al, 2005). Results of the MIM analysis may document the link between volcanic activity and hydrothermal recharge events in HSBV.

This work clarifies some of the outstanding questions in the literature considering HSBV and Akutan volcano. Stelling et al. (2015) interpreted the geothermal reservoir to be approximately below the fumaroles at the head of the upper arm of HSBV. Kolker et al. (2012) proposed two possible outflow paths either to the south and east following the valley floor or north and east under Mt. Formidable. DeGrandpre et al., (2017) used geodetic data from five time frames (pre-2008, 2009-2013, 2014, and post 2014) to model sources of inflation. Low V_p and a high V_p/V_s values from Syracuse et al., (2015) and high rates of vertical displacement recorded during 2008 and 2014 with no subsidence documented after either inflation event indicates that a large amount of magma ($\sim 0.2\text{km}^3$) is being stored in a mush zone centered beneath the northeastern rim of the caldera at 7-8km depth (Figure 24) (Syracuse et al., 2015; DeGrandpre et al., 2017). Injection or removal of material from this long term storage chamber causes brittle deformation at its edges (Syracuse et al., 2015), as seen during the 1996 dike emplacement that removed material from the magma chamber resulting in the seismic swarm. From this work I can add that in the vicinity of HSBV normal faulting on NW trending faults is linked to the brittle deformation caused by removal of material from this shallow magma chamber and has the effect of creating permeable inflow pathways to the hydrothermal system possibly contributing the increased energy output that (Bergfeld et al., 2014) recorded. However, permeability is not the only thing responsible for increased energy output in hydrothermal systems. (Bergfeld et al., 2014) attributed the increase in heat output to the 1996 event, such longevity would require a large addition of heat. The episodic injections modeled by DeGrandpre et al., (2017) have likely added heat to the HSBV system multiple times throughout the last decade and Syracuse et al. (2015) has documented relatively little seismicity in HSBV since 1996. Therefore, magmatic heat is being added with little fracturing

and therefore only modest increases in permeability since the 1996 event. Based on the record of sustained volcanic activity at Akutan, it is likely that this process of relatively aseismic magma injection from depth and shallow brittle failure from dike injection will continue in the future.

Because well TG-4 is located on the southern periphery of the inflow and outflow systems I can only speculate about the structures that conduct the heated geothermal fluids from the reservoir to the surface. It is possible that the outflow is diffuse, utilizing the network of NW and NNE trending faults that repeatably rupture because of tectonic stresses. Furthermore, weak lithologies likely accommodate fracturing and concentrate the outflow into sheets. There are three prominent structural orientations mapped on the surface surrounding the TG-4 site (WNW/ESE, NE/SW, and E/W). Cross-cutting relation data (Figure 16.F) include veins with NW/SE, N/S, and a smaller number of E/W and NE/SW orientations. The relative lack of E/W and NE/SW trending structures in the core could indicate that the E/W and NE/SW trending structures are inactive at the TG-4 locality. The NE trending line of hot springs in HSBV (Figure 1, Figure 24) defines a proposed fault (Stelling et al. 2015). Syracuse et al. (2015) reported relocated seismic epicenters at around 6km depth along the same trend but slightly SE of the proposed NE trending fault. This may suggest a SE dipping fault parallel to the valley wall. The southeastern block of the proposed NE trending fault might be an impermeable layer that concentrates the diffuse flow, as there are no hot springs to the south of the proposed fault. Further analysis of the wells located in the outflow path, TG-2 and TG-3, is necessary in order to test these ideas.

Works Cited

- Allerton, S.A., McNeill, A.W., Stokking, L.B., Pariso, J.E., Tartarotti, P., Marton, F.C., and Pertsev, N.N., 1995, Structures and magnetic fabrics from the lower sheeted dike complex of Hole 504B reoriented using stable magnetic remanence, *in* Proceedings of the Ocean Drilling Program, Scientific Results, v. 137, p. 245–251.
- Angelier, J., 1984, Tectonic analysis of fault slip data sets: *Journal of Geophysical Research: Solid Earth*, v. 89, p. 5835–5848.
- Ave Lallemand, H.G., and Oldow, J.S., 2000, Active displacement partitioning and arc-parallel extension of the Aleutian volcanic arc based on Global Positioning System geodesy and kinematic analysis: *Geology*, v. 28, p. 739–742.
- Bergfeld, D., Lewicki, J.L., Evans, W.C., Hunt, A.G., Revesz, K., and Huebner, M., 2014, Geochemical investigation of the hydrothermal system on Akutan Island, Alaska, July 2012: U.S. Geological Survey Scientific Investigations Report Scientific Investigations Report.
- Byers, F.M., and Barth, T.F.W., 1953, Volcanic activity on Akun and Akutan islands: *Proceedings Seventh Pacific Science Congress*, v. 2.
- DeGrandpre, K., Wang, T., Lu, Z., and Freymueller, J.T., 2017, Episodic inflation and complex surface deformation of Akutan volcano, Alaska revealed from GPS time-series: *Journal of Volcanology and Geothermal Research*, v. 347, p. 337–359.
- Demarest, H. H., 1983, Error analysis for the determination of tectonic rotation from paleomagnetic data: *Journal of Geophysical Research: Solid Earth*, v. 88(B5), p. 4321–4328.
- Drummond, S.E., and Ohmoto, H., 1985, Chemical evolution and mineral deposition in boiling hydrothermal systems: *Economic Geology*, v. 80, p. 126–147.
- Dunlop, D.J., 2002, Theory and application of the Day plot (M_{rs} / M_s versus H_{cr} / H_c) 1. Theoretical curves and tests using titanomagnetite data: *Journal of Geophysical Research*, v. 107, p. 2056.
- Elders, W.A., Hoagland, J.R., and Williams, A.E., 1981, Distribution of hydrothermal mineral zones in the Cerro Prieto geothermal field of Baja California, Mexico: *Geothermics*, v. 10, p. 245–253.
- Fay, G., Meléndez, A.V., and West, C., 2013, Alaska Energy Statistics 1960-2011 Final Report p. 72.
- Finch, R.H., 1935, Akutan volcano: *Volcanological Review*, v. 16, p. 155–160.
- Fisher Ronald Aylmer, 1953, Dispersion on a sphere: *Proceedings of the Royal Society of London. Series A. Mathematical and Physical Sciences*, v. 217, p. 295–305.

- Fuller, M., 1969, Magnetic orientation of borehole cores: *Geophysics*, v. 34, p. 772–774.
- Hailwood, E.A., and Ding, F., 1995, Palaeomagnetic reorientation of cores and the magnetic fabric of hydrocarbon reservoir sands: Geological Society, London, Special Publications, v. 98, p. 245–258.
- Hill, I.A., Taira, A., Firth, J.V., and et al. (Eds.), 1993, Proceedings of the Ocean Drilling Program, 131 Scientific Results: Ocean Drilling Program, Proceedings of the Ocean Drilling Program, v. 131.
- Johnson Catherine L., and Constable Catherine G., 1996, Palaeosecular variation recorded by lava flows over the past five million years: *Philosophical Transactions of the Royal Society of London. Series A: Mathematical, Physical and Engineering Sciences*, v. 354, p. 89–141.
- Kent, D.V., Olsen, P.E., and Witte, W.K., 1995, Late Triassic-earliest Jurassic geomagnetic polarity sequence and paleolatitudes from drill cores in the Newark rift basin, eastern North America: *Journal of Geophysical Research*, v. 100, p. 14,965–14,998.
- Kirschvink, J.L., 1980, The least-squares line and plane and the analysis of palaeomagnetic data: *Geophysical Journal International*, v. 62, p. 699–718.
- Kolker, A., Bailey, A., and Howard, W., 2011, The 2010 Akutan Exploratory Drilling Program: Preliminary Findings: *Geothermal Resource Council Transactions*, v. 35, p. 847–852.
- Kolker, A., Stelling, P., Cumming, W., and Rohrs, D., 2012, Exploration of the Akutan geothermal resource area, *in* Proceedings, Thirty-Seventh Workshop on Geothermal Reservoir Engineering, v. 37.
- Lu, Z., Wicks Jr, C., Kwoun, O., Power, J.A., and Dzurisin, D., 2005, Surface deformation associated with the March 1996 earthquake swarm at Akutan Island, Alaska, revealed by C-band ERS and L-band JERS radar interferometry: *Canadian Journal of Remote Sensing*, v. 31, p. 7–20.
- Lurcock, P.C., and Wilson, G.S., 2012, PuffinPlot: A versatile, user-friendly program for paleomagnetic analysis: *Geochemistry, Geophysics, Geosystems*, v. 13.
- Maxbauer, D.P., Feinberg, J.M., and Fox, D.L., 2016, MAX UnMix: A web application for unmixing magnetic coercivity distributions: *Computers & Geosciences*, v. 95, p. 140–145.
- Miller, T.P., McGimsey, R.G., Richter, D.H., Riehle, J.R., Nye, C.J., Yount, M.E., and Dumoulin, J.A., 1998, Catalog of the historically active volcanoes of Alaska: US Geological Survey Open-File Report, v. 98, p. 582.
- Motyka, R.J., Liss, S.A., Nye, C.J., and Moorman, M.A., 1993, Geothermal resources of the Aleutian arc: Division of Geological and Geophysical Surveys.

- Richter, D.H., Waythomas, C.F., McGimsey, R.G., and Stelling, P.L., 1998, Geology of Akutan Island, Alaska: US Geological Survey Open-File Report, p. 98–135.
- Romick, J.D., Perfit, M.R., Swanson, S.E., and Shuster, R.D., 1990, Magmatism in the eastern Aleutian arc: temporal characteristic of igneous activity on Akutan Island: *Contributions to Mineralogy and Petrology*, v. 104, p. 700–721.
- Simón, J.L., 2018, Forty years of paleostress analysis: has it attained maturity?: *Journal of Structural Geology*, doi:10.1016/j.jsg.2018.02.011.
- Sperner, B., and Zweigel, P., 2010, A plea for more caution in fault–slip analysis: *Tectonophysics*, v. 482, p. 29–41.
- Stelling, P., Hinz, N.H., Kolker, A., and Ohren, M., 2015, Exploration of the Hot Springs Bay Valley (HSBV) geothermal resource area, Akutan, Alaska: *Geothermics*, v. 57, p. 127–144.
- Stone, D.B., and Layer, P.W., 2006, Paleosecular variation and GAD studies of 0-2 Ma flow sequences from the Aleutian Islands, Alaska: *PALEOSECULAR VARIATION: Geochemistry, Geophysics, Geosystems*, v. 7.
- Syracuse, E.M., Maceira, M., Zhang, H., and Thurber, C.H., 2015, Seismicity and structure of Akutan and Makushin Volcanoes, Alaska, using joint body and surface wave tomography: *Journal of Geophysical Research: Solid Earth*, v. 120, p. 1036–1052.
- Yamaji, A., 2000, The multiple inverse method: a new technique to separate stresses from heterogeneous fault-slip data: *Journal of Structural Geology*, v. 22, p. 441–452.

Tables

Table 1: Results of demagnetization analysis for selected sites in core TG4

Site (m)	Sample (Cooling unit)	Specimen	Demagnetization method	Magnetometer	Max T (°C)	Max Field (mT)	Number of components	Observations	Interpretation	Chosen Vector (deg)		MAD ₃ (deg)
										Inclination	Declination	
179.4 - 181.5	Andesite	589-2A	AF	Cryo		90	2	1 st components is horizontal, 2 nd steeply inclined. Specimen B,C, F have I>85	1 st component is sampling overprint. 2 nd component is ChRM held by magnetite	-82.62	218.07	0.72
		589-2B	AF	Cryo		90	2			-	-	-
		589-2C	Thermal	Cryo	600		2			-	-	-
		589-2D	AF	Cryo		90	2			-84.94	155.22	0.58
		589-2E	Thermal	Spinner	568		2			-81.29	131.11	0.51
		589-2F	AF	Spinner		100	2			-	-	-
	Basalt	594-2A	Thermal	Spinner	602		2	1 st components are random. 2 nd components are consistant.	2 nd is ChRM held by magnetite	-69.98	155.9	0.59
		594-2B	AF	Spinner		70	2			-	-	-
		594-2C	Thermal	Spinner	602		2			-69.98	145.74	3.34
		594-2D	AF	Spinner		90	2			-72.62	136.29	1.52
		594-2E	Thermal	Spinner	602		2			-63.26	126.11	0.55
		594-2F	AF	Spinner		110	2			-60.63	114.31	2.18
253.1 - 256.3	Basalt	839-1.5A	AF	Cryo		70	2	1 st is vertical, 2 nd are consistent.	2 nd is ChRM held by magnetite	-65.65	4.29	1.36
		839-1.5B	Thermal	Cryo	600		2			-58.05	1.7	0.67
		839-1.5C	AF	Cryo		70	2			-57.57	357.07	2.16
		839-2A	Thermal	Cryo	600		2			-63.44	13.45	1.31
		839-2B	AF	Cryo		70	2			-67.45	0.3	1.06
287.1 - 299.6	Andesite	947-10A	AF	Cryo		60	2	Inclination is lower than 60°	Sequence no longer in original position	-	-	-
		947-10B	AF	Cryo		70	2			-	-	-
		947-10C	AF	Cryo		70	2			-	-	-
	Andesite	955-9A	AF	Cryo		70	1	Alternating D between specimens	Sampling overprint	-	-	-
		955.5-11A	AF	Cryo		70	1			-	-	-
		955.5-11B	AF	Cryo		70	1			-	-	-
	Basalt	957-15A	AF	Spinner		35	2	Vertical 1 st component, inconsistant 2 nd component	DIRM	-	-	-
		957-15B	AF	Cryo		40	2			-	-	-
		957-15C	AF	Cryo		40	2			-	-	-
	Andesite	965.5-11A	Thermal	Cryo	395		2	1 st component is consistent with 2 nd component in 971-2. 2 nd component has I >85°	Basalt at 971 intruded and overprinted Andesite	73.03	248.45	1.67
		965.5-11B	AF	Cryo		35	2			82.44	209.03	1.69
		965.5-11C	Thermal	Cryo	420		2			71.86	247.82	5.24
		965.5-11D	AF	Cryo		30	1			-	-	-
		965.5-11E	Thermal	Cryo	449		2			69.46	234.93	5.47
		965.5-11F	AF	Cryo		30	2			79.59	214.89	2.73
Basalt	971-2A	AF	Spinner		20	2	1 st and 2 nd D are similar. I between 64° and 75°	2 nd component is ChRM	75.91	186.83	0.74	
	971-2B	AF	Cryo		50	2			69.54	207.82	4.52	
	971-2C	AF	Spinner		35	2			64.1	212.88	2.24	
311.7 - 313.9	Basalt	1024-2A	Thermal	Spinner	569		1	1 st components are vertical, 2 nd are consistent.	1 st component is DIRM. 2 nd component is ChRM	-	-	-
		1024-2B	Thermal pilot	Spinner	570		1			74.9	240.65	1.19
		1024-2C	AF	Spinner	570		2			79.28	177.02	1.7
		1024-2D	Thermal	Spinner		15	2			75.78	226.31	1.55
		1024-2E	AF	Spinner	570		2			-	-	-
		1024-2F	Thermal	Spinner		15	2			-	-	-
313.9 - 324.9	Basalt	1041-16A	Thermal	Cryo	500		3	1 st and 2 nd component has I similar to modern I and varied D. 3 rd component is Reverse	1 st and 2 nd components are sampling and or DIRM. 3 rd component is ChRM	-64.67	200.39	1.93
		1041-16B	AF	Cryo		15	1			-	-	-
		1041-16C	Thermal	Cryo	390		3			-53.07	207.69	4.73
		1041-16D	AF	Cryo		15	1			-	-	-
		1041-16E	Thermal	Cryo	500		2			-	-	-
		1041-16F	AF	Cryo		15	1			-	-	-
	Gabbro	1042-1A	AF	Cryo		40	2	1 st has I similar to modern. 2 nd is reverse	1 st component is DIRM. 2 nd is ChRM	-61.48	210.22	4.66
		1042-1B	AF	Cryo		40	2			-75.92	211.83	2.88
		1042-1C	AF	Cryo		40	2			-72.98	214.96	3.72
	Andesite	1053-4A	AF	Cryo		40	2	1 st and 2 nd are almost indistinguishable	DIRM or ChRM	-	-	-
		1053-4B	AF	Spinner		50	2			-	-	-
	Andesite	1064-4A	AF	Spinner		50	2	Inclination is near vertical	DIRM	-	-	-
		1064-4B	AF	Spinner		30	2			-	-	-
		1064-4C	AF	Spinner		30	2			-	-	-
	Basalt	1065-16A	AF	Spinner		30	2	1 st component is vertical, 2 nd is consistant with 2 nd component at 1053	1 st is DIRM. 2 nd could be ChRM	-	-	-
1065-16B		AF	Spinner		30	2	-			-	-	
1065-16C		AF	Spinner		25	2	-			-	-	

Note: Full list of sites listed in appendix B. Cryo= cryogenic magnetometer. Max T= maximum temperature (C°) reached in thermo-demagnetization. Max Field= maximum magnetic field (mT) reached in alternating field demagnetization. In observation and interpretation columns I= inclination, D= declination. A (-) in the Chosen vector columns indicates no vector was used from that sample. The maximum angular deviation (MAD3) angle is a measure of data alignment in a vector, with smaller angles indicating less spread in the data.

Table 2. Inclination and declination of site means calculated by fisher statistics

Site (m)	Inclination (deg)	Declination (deg)	Lower Hemisphere Corrected		Alpha95 of site (deg)	k of site	Rotational Error (± deg)
			Inclination (deg)	Declination (deg)			
179.4 - 181.5	-74.4	137.6	74.4	317.6	7.8	51.0	21.5
253.1 - 256.3	-62.6	3.1	62.6	183.1	5.0	232.7	18.5
287.1 - 299.6	74.2	221.9	-	-	5.8	92.8	22.2
311.7 - 313.9	77.9	219.3	-	-	11.3	120.4	9.9
313.9 - 324.9	-65.7	208	65.7	28	8.9	74.3	21.3

Note: Alpha95 is the radius of 95% confidence. The precision parameter (k) is a measure of dispersion with higher values indicating more tightly clustered directions.

Table 3. Results of the multiple inverse method on shear veins separated by mineralogy.

Data Set	Orientation Group	Φ	Sigma 1		Sigma 3		Azimuth Error (\pm°)
			Trend	Plunge	Trend	Plunge	
4-5 high conf	1	0.4	349.0	0.0	259.0	0.0	20.7
	2	0.4	347.9	0.0	78.0	29.0	
	3	0.1	205.2	51.2	80.1	24.7	
		0.6	230.4	58.5	79.1	28.2	
	4	1	164.2	41	38.6	33.8	
	5	0.2	343.1	33.8	237	22.7	
		0.3	325.3	55.3	235.3	0	
		0.5	330	50.8	226.5	10.9	
0.8		326	36.6	216	24.4		
All chl	1	0.2	347.1	0	257	0	21.5
	2	0.3	345.4	0	75.4	25	
	3	0.2	207.4	50.5	82.6	25.2	
		0.5	136.6	38.5	31.1	18.6	
		0.8	179.8	47.2	71.6	16.1	
chl+cal	1	0.4	344.7	0	254.7	0	21.8
	2	0.4	347.4	0	77.4	24.7	
	3	0.2	209	47.4	85.5	26.9	
		0.6	217.4	61.8	78	22.2	
		0.8	183.3	48.7	72.4	17.4	
All cal (no chl)	4	1	284.9	32.9	37.3	30.6	19.7
	5	0	8.5	61.7	222.9	24	
		0.1	344.6	29.5	236.9	28.4	
		0.2	346.2	32.6	248.5	11.7	
		0.3	337.3	45.6	240.2	6.7	
		0.4	336	66.4	231.2	6.3	
		0.5	336.4	51.5	237.7	6.8	
		0.6	340.8	42.7	231.6	19.5	
0.7	317.2	22.9	54.7	17.3			

Table A1. List of sample masses.

Sample	Mass (kg)	Sample	Mass (kg)	Sample	Mass (kg)
414.5Ch	1.07E-04	965Ch	3.69E-05	1107Ch	5.02E-05
414.5P	1.16E-04	965P	5.36E-05	1107P	7.43E-05
589Ch	3.53E-05	971Ch	1.03E-04	1161Ch	2.04E-05
589P	1.20E-04	971P	1.34E-04	1161P	1.10E-04
828Ch	1.07E-04	1042Ch	3.88E-05	1271Ch	5.12E-05
828P	1.19E-04	1042P	1.20E-04	1271P	8.65E-05

Note: Sample weights in kg, for representative samples. Samples are named by depth in feet with postscript P=powdered and Ch=chip samples.

Figures

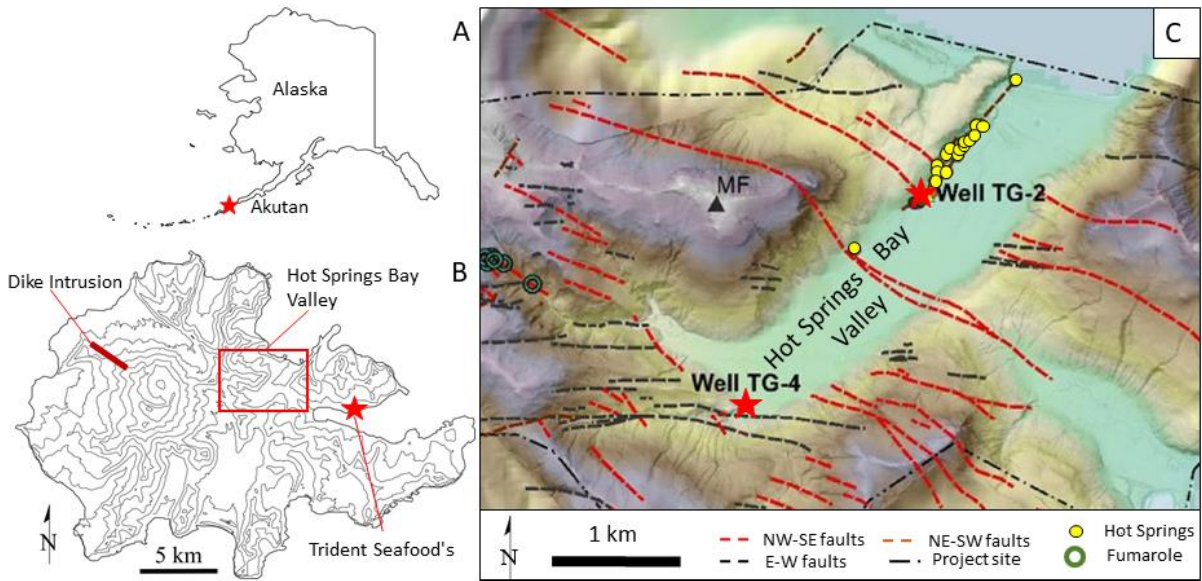


Figure 1. Map of A) Akutan in relation to Alaska denoted by the red star; B) the location of Hot Springs Bay valley (HSBV), on Akutan Island (red box) and Trident Seafoods processing plant (red star); C) the location of well TG-4 and structural and geothermal features within HSBV. MF = Mt. Formidable. Modified from Stelling et al. 2015.

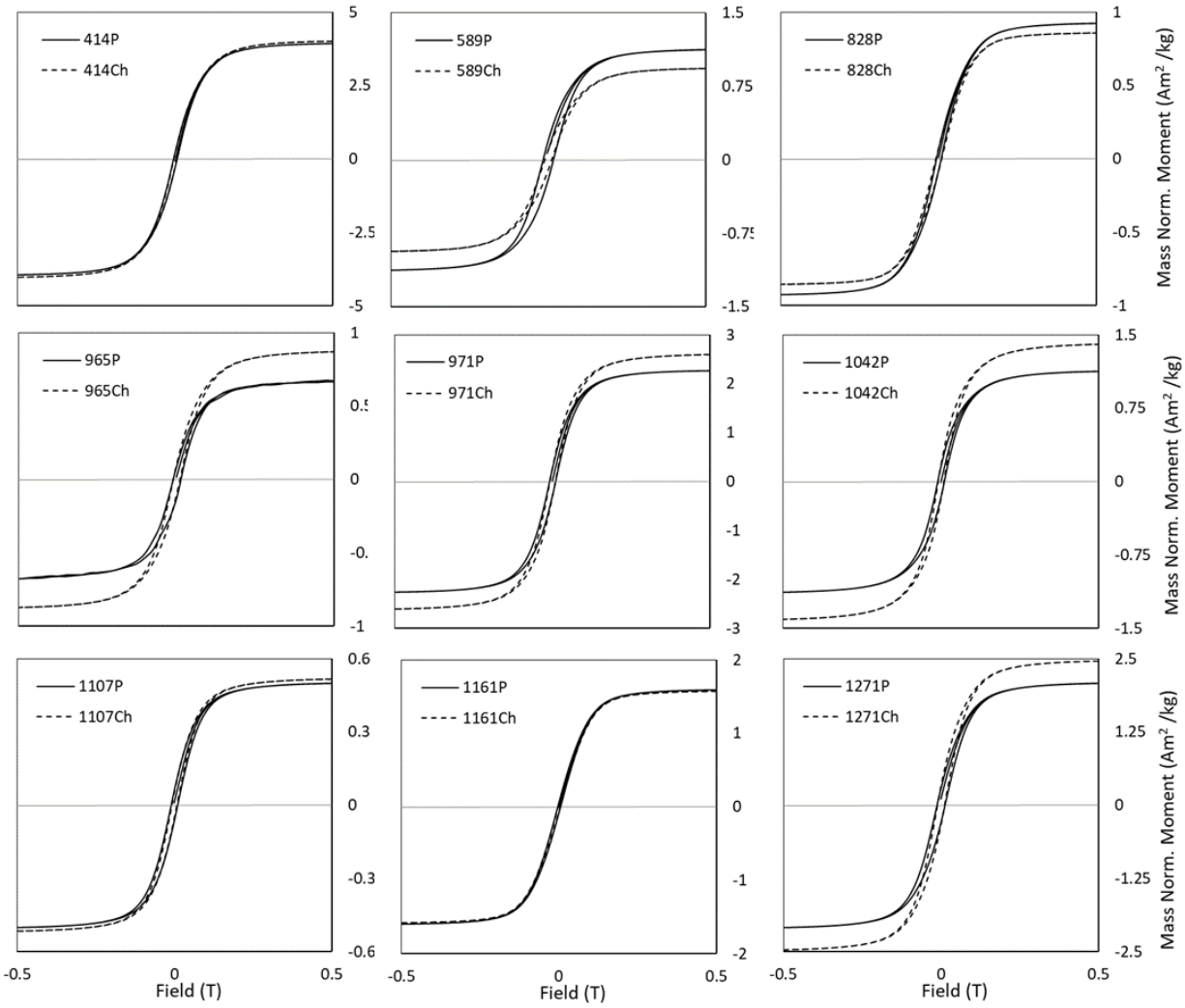


Figure 2. Mass normalized hysteresis loops with high field corrections for representative samples. Samples are named by depth in feet with postscript P=powdered and Ch=chip samples. See appendix A for full laboratory procedure.

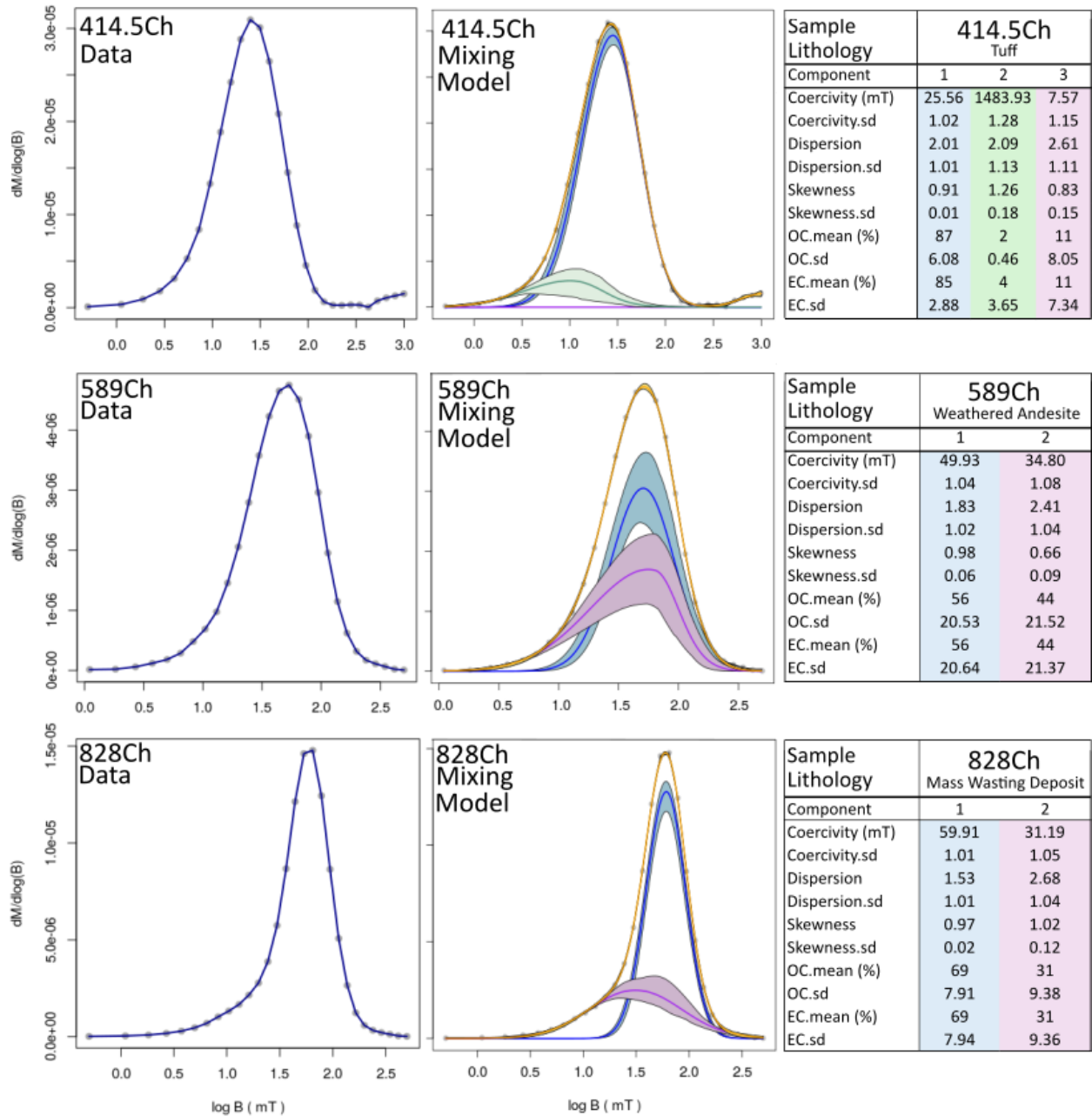


Figure 3. IRM data (left column) and results of unmixing of IRM curves (center and right columns) for representative samples. In the center column the magnetic components are represented by the different colored curves, the mean result is denoted by the dark central lines and the 95% confidence limits by the lighter shaded regions. Black points are the original data and the yellow curve is the model. Numerical results (right column) of unmixed IRM curves for representative chip samples are highlighted in the color that corresponds to component curves in the center column. OC=observed contribution. EC=extrapolated contribution. The “.sd” is the standard deviation of error of whatever precedes it. Samples are named by depth in feet with the postscripts Ch=chip sample.

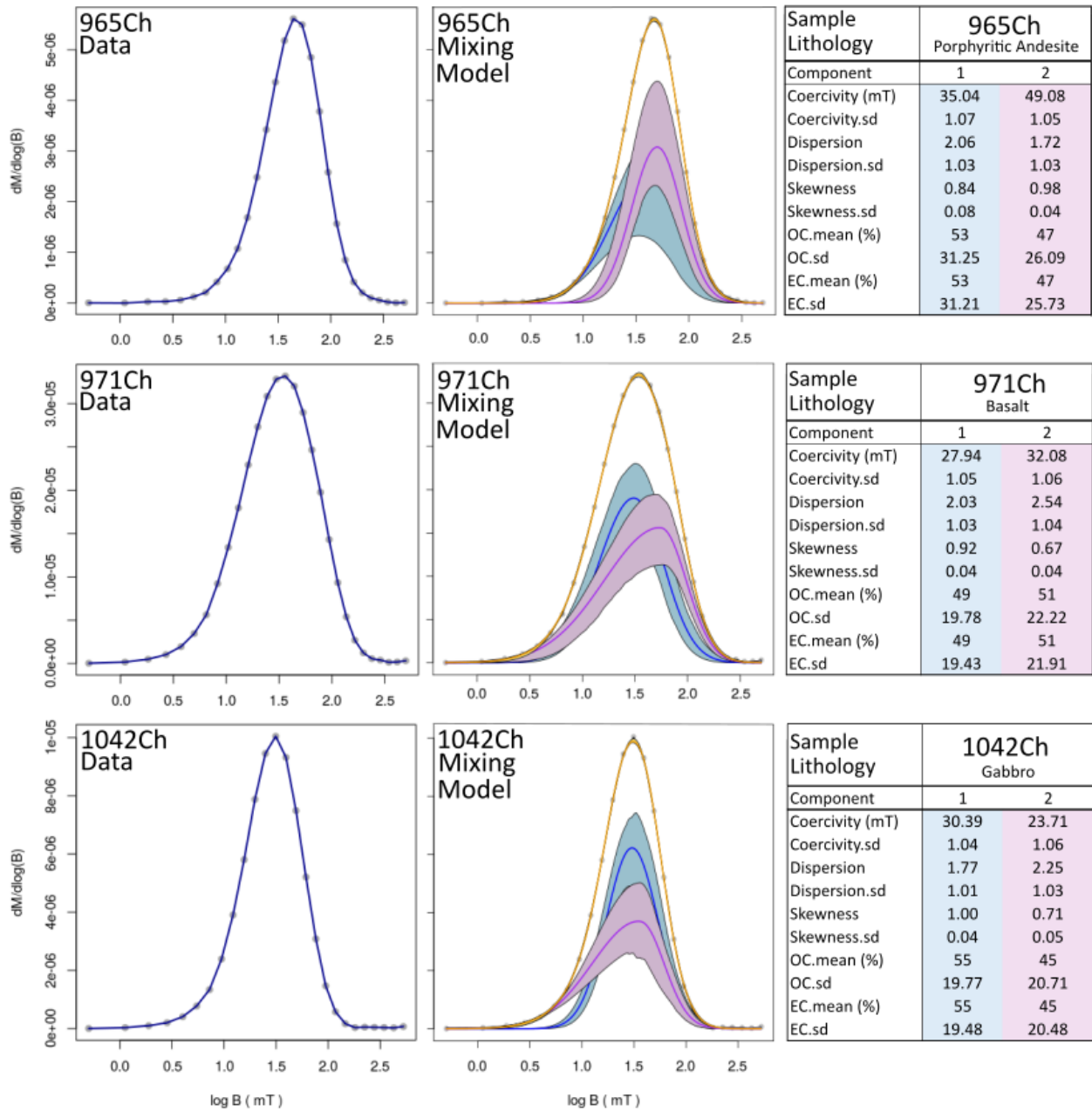


Figure 3. Continued

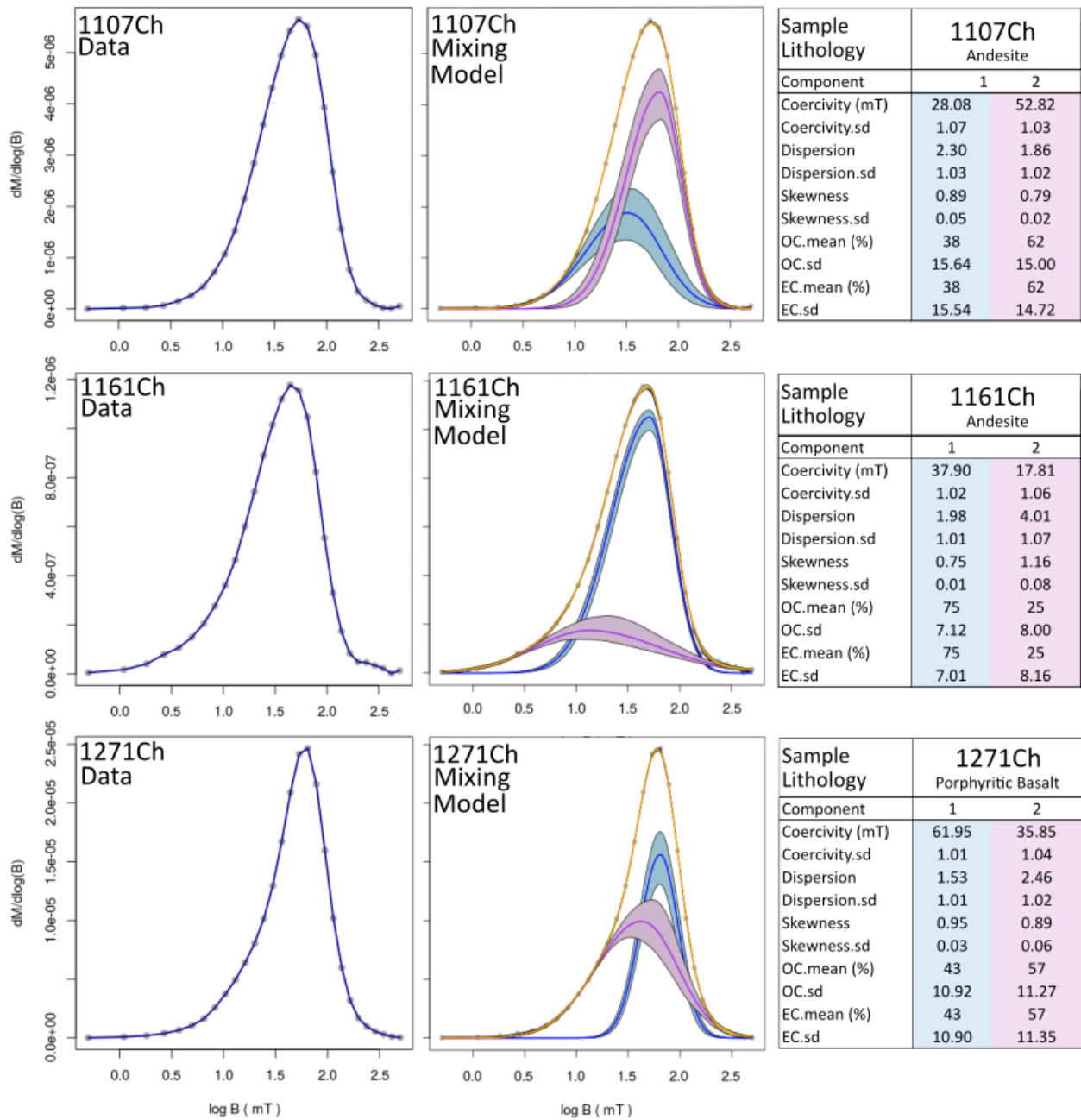


Figure 3. Continued

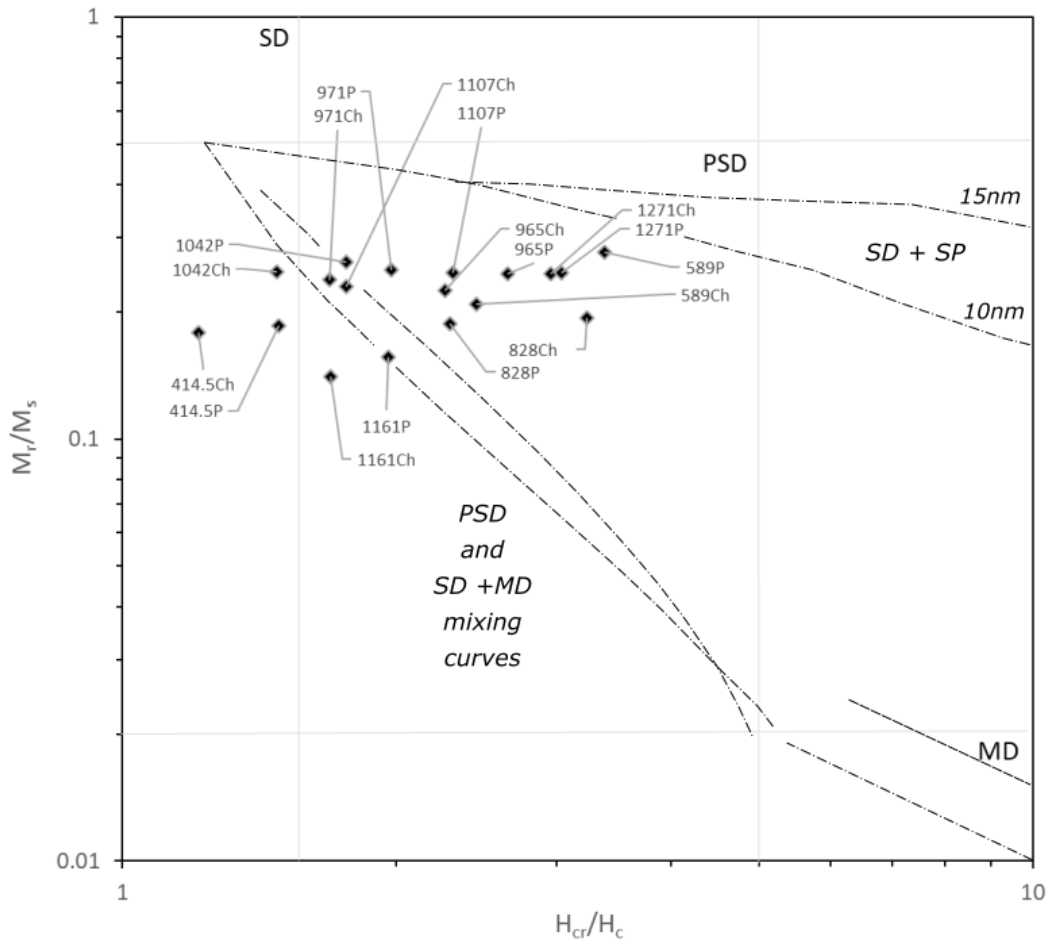


Figure 4. Day plot of representative samples from HSBV. SD=single-domain, PSD= pseudosingle-domain, MD=multi=domain. Mixing curves for magnetite (dash-double-dot lines) are presented following the theory of Day et al. (1977) after Dunlop (2002).

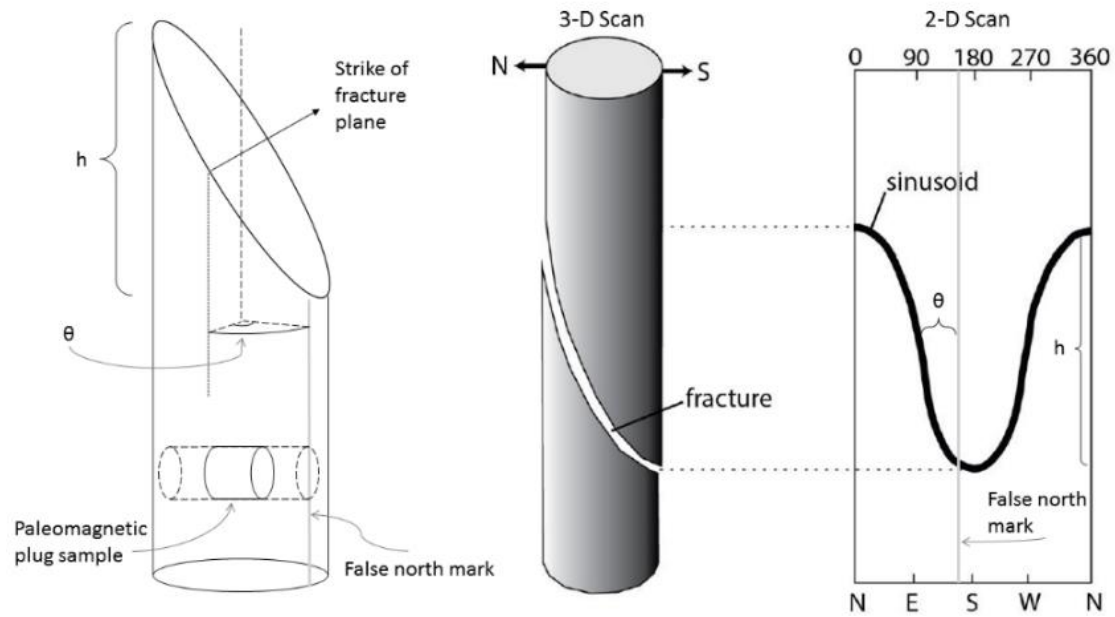


Figure 5. Cartoon showing the position of plug samples for paleomagnetic analysis relative to the false north mark (N'), and a representation of fractures in the 3-D and "unrolled" 2-D states. The height (h) of the sinusoid and the distance from N' to the inflection point (θ) are used to calculate the strike and dip of structural features from the 2-D scans.

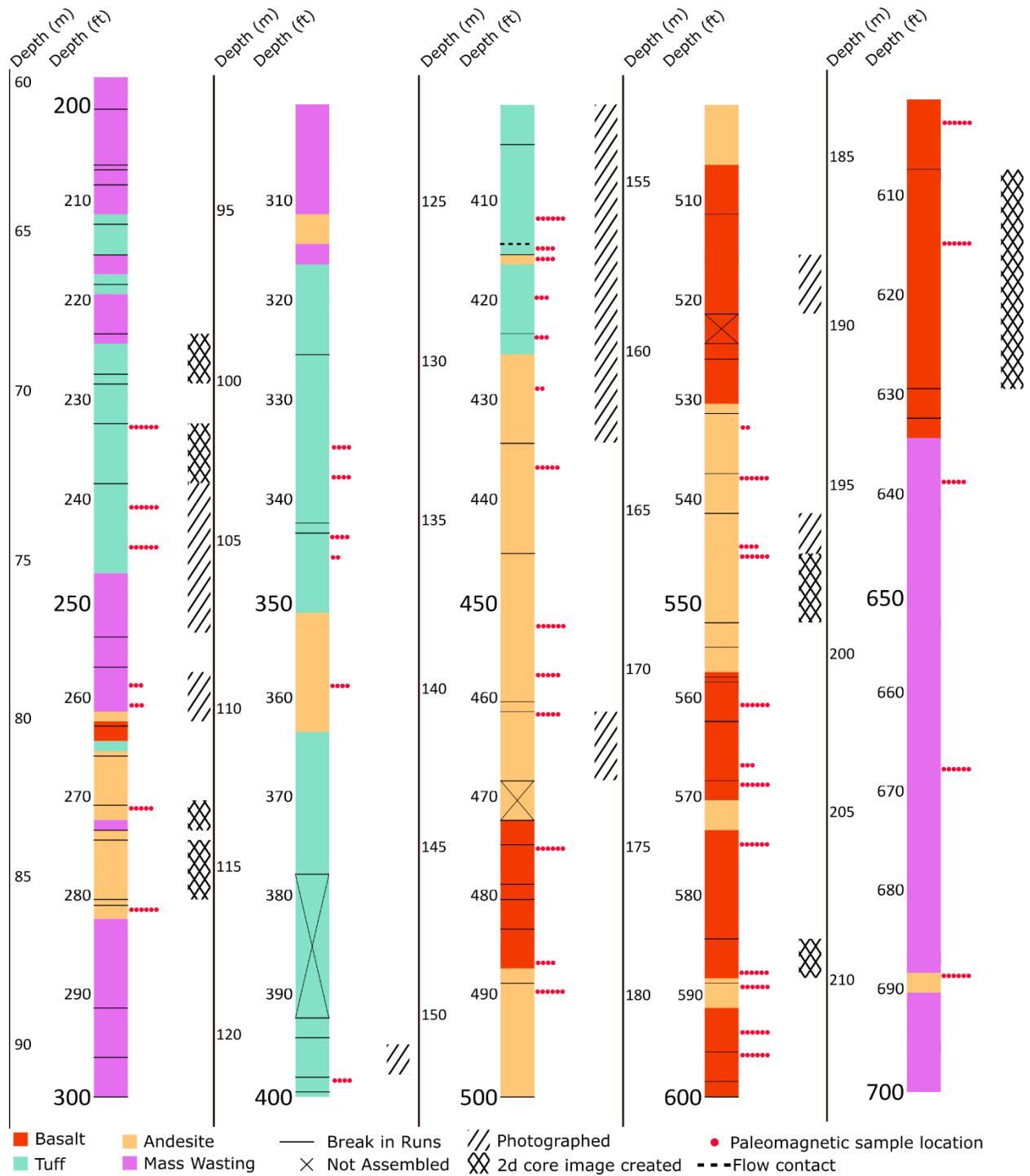


Figure 6. Core log of well TG-4 showing lithology (colored blocks), breaks in run lengths (horizontal black lines), flow contacts between like lithologies (dashed lines), depth intervals of core that were not reassembled (i.e. no N' mark) (exed out), number of samples for paleomagnetic analysis and their location (red circles), depth intervals of core that have been photographed (slanted lines), and depth intervals where 2d core images have been created (cross hatch).

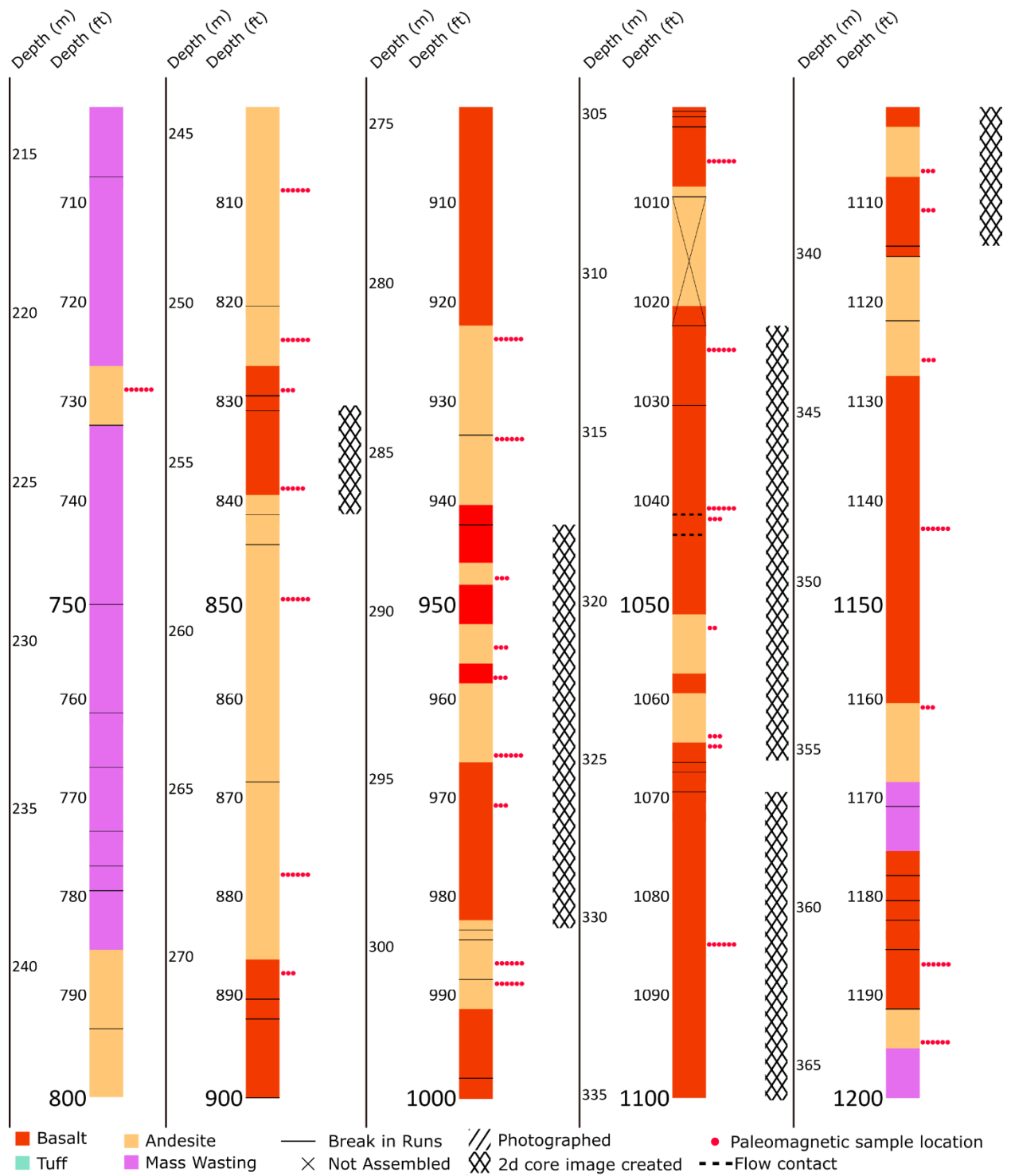


Figure 6. Continued.

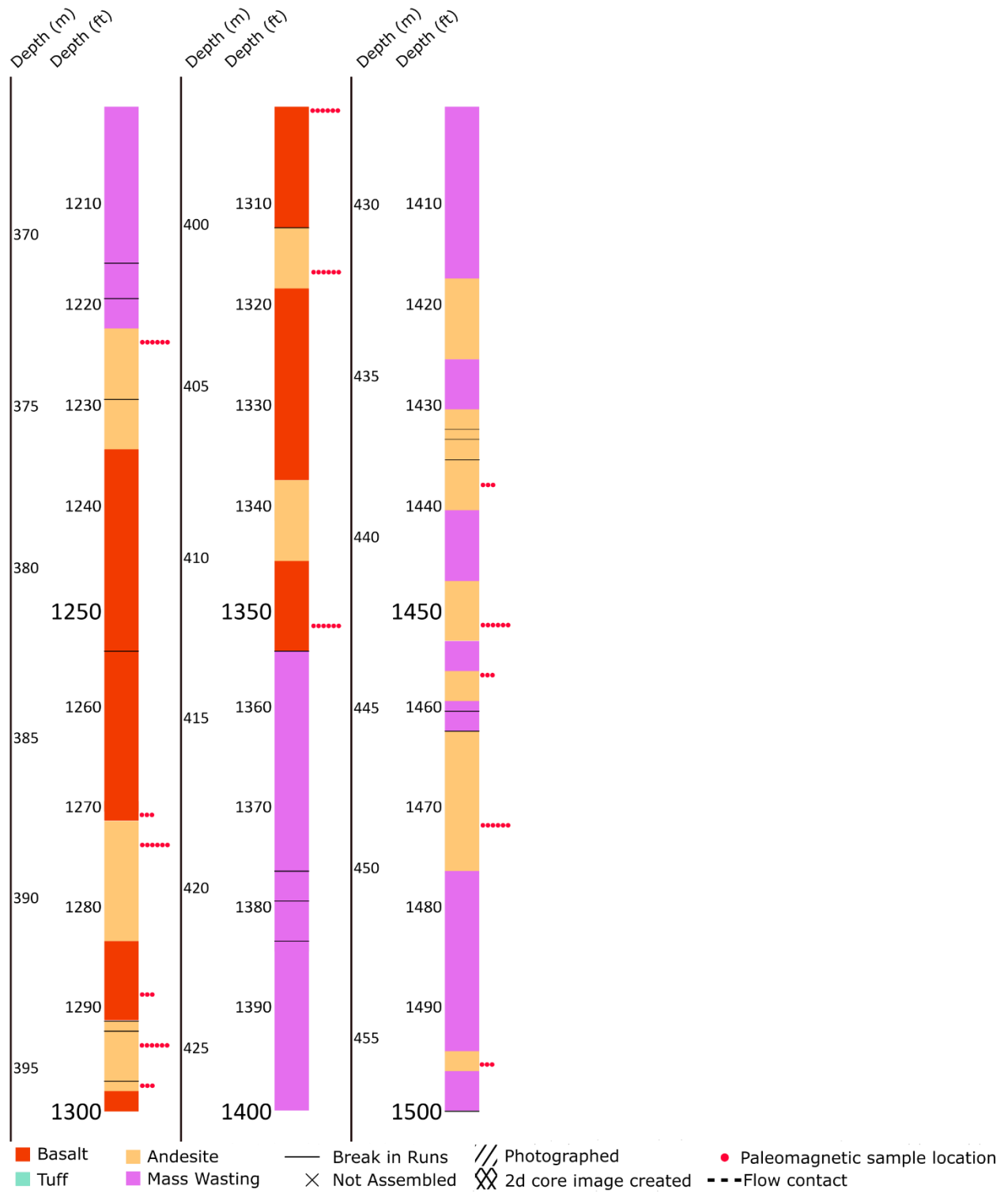


Figure 6. Continued.

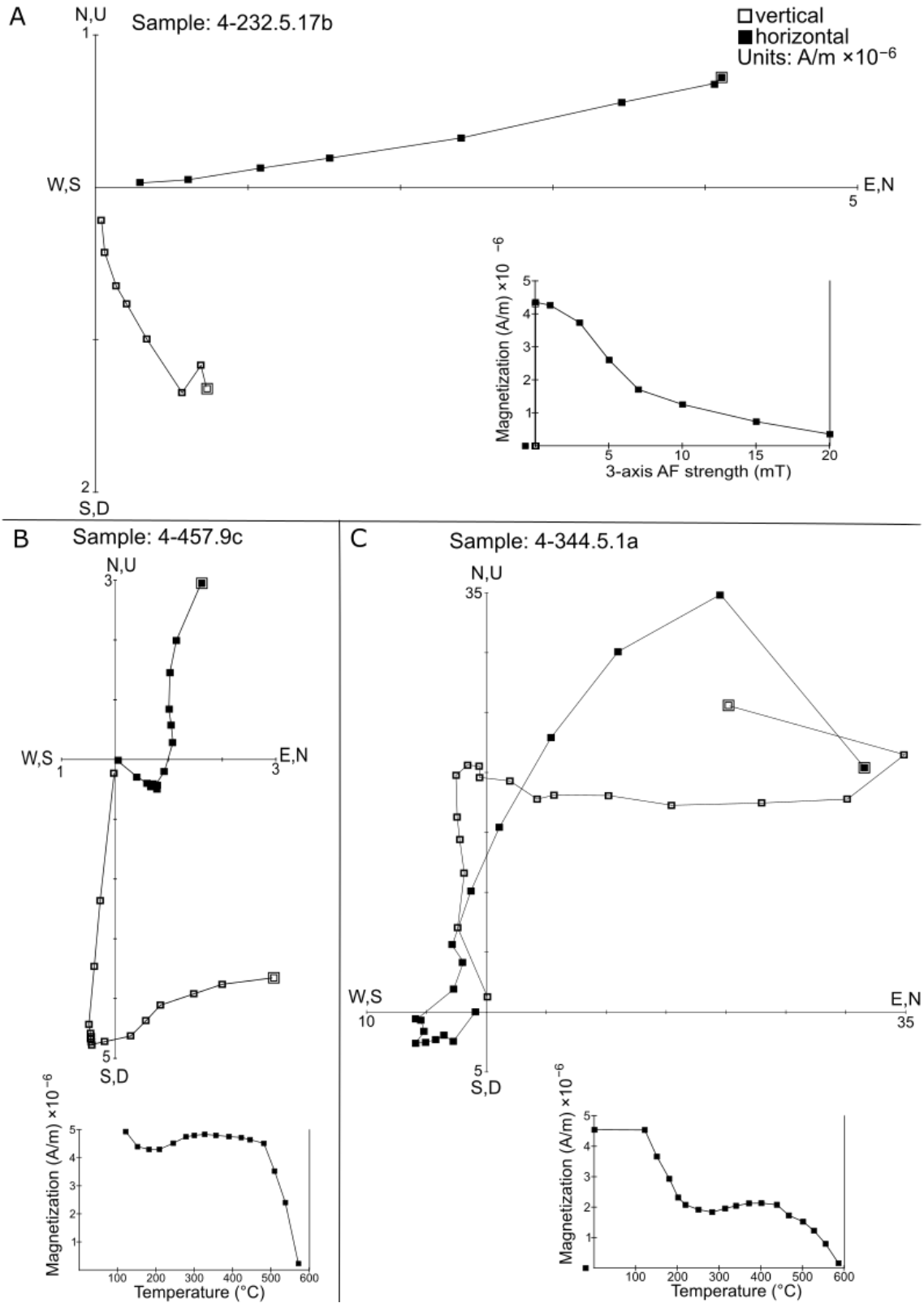


Figure 7. Zijderveld plots and demagnetization curves for representative components within the tuff lithology.

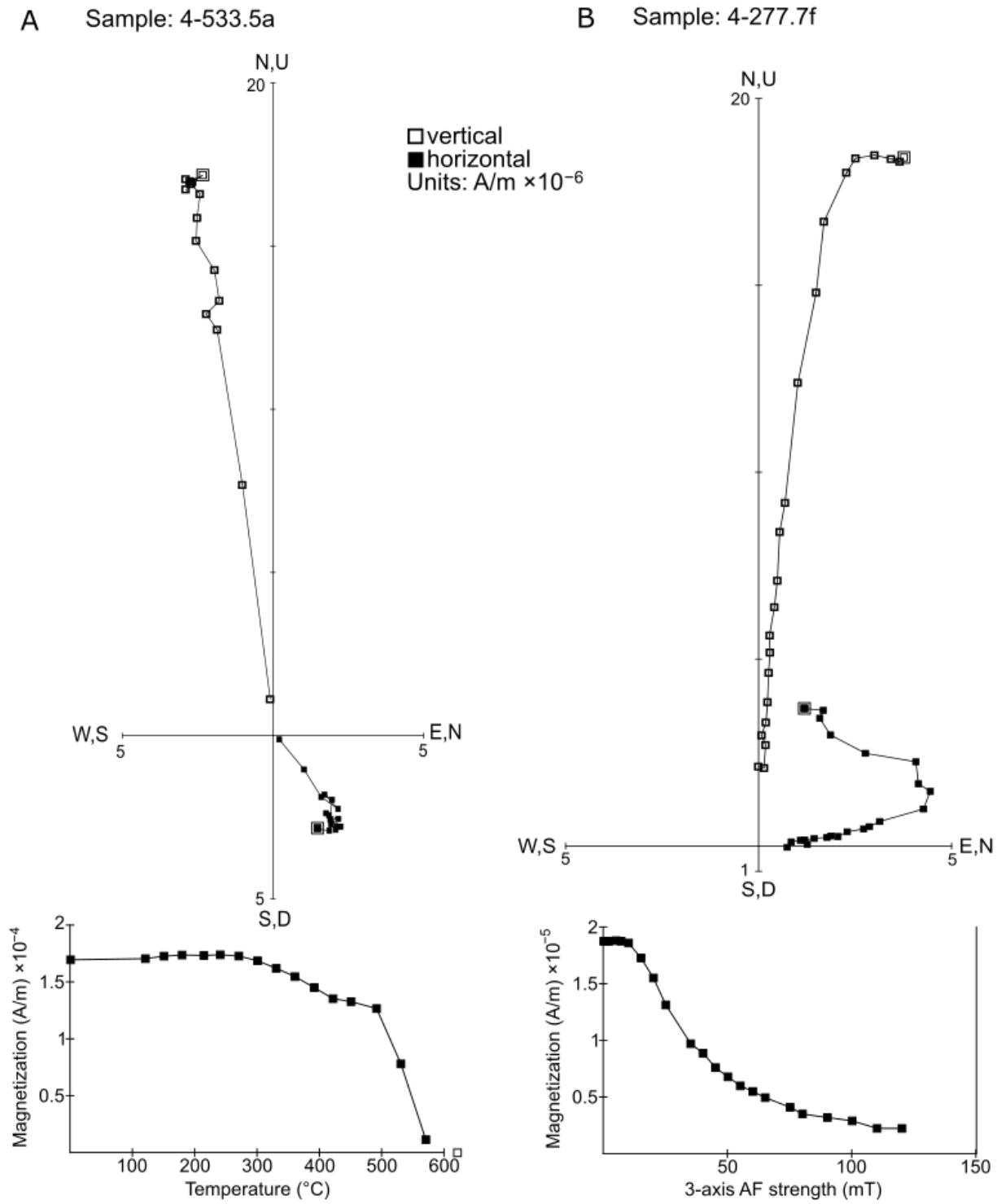


Figure 8. Zijderveld plots and demagnetization curves for representative components within the andesite lithology.

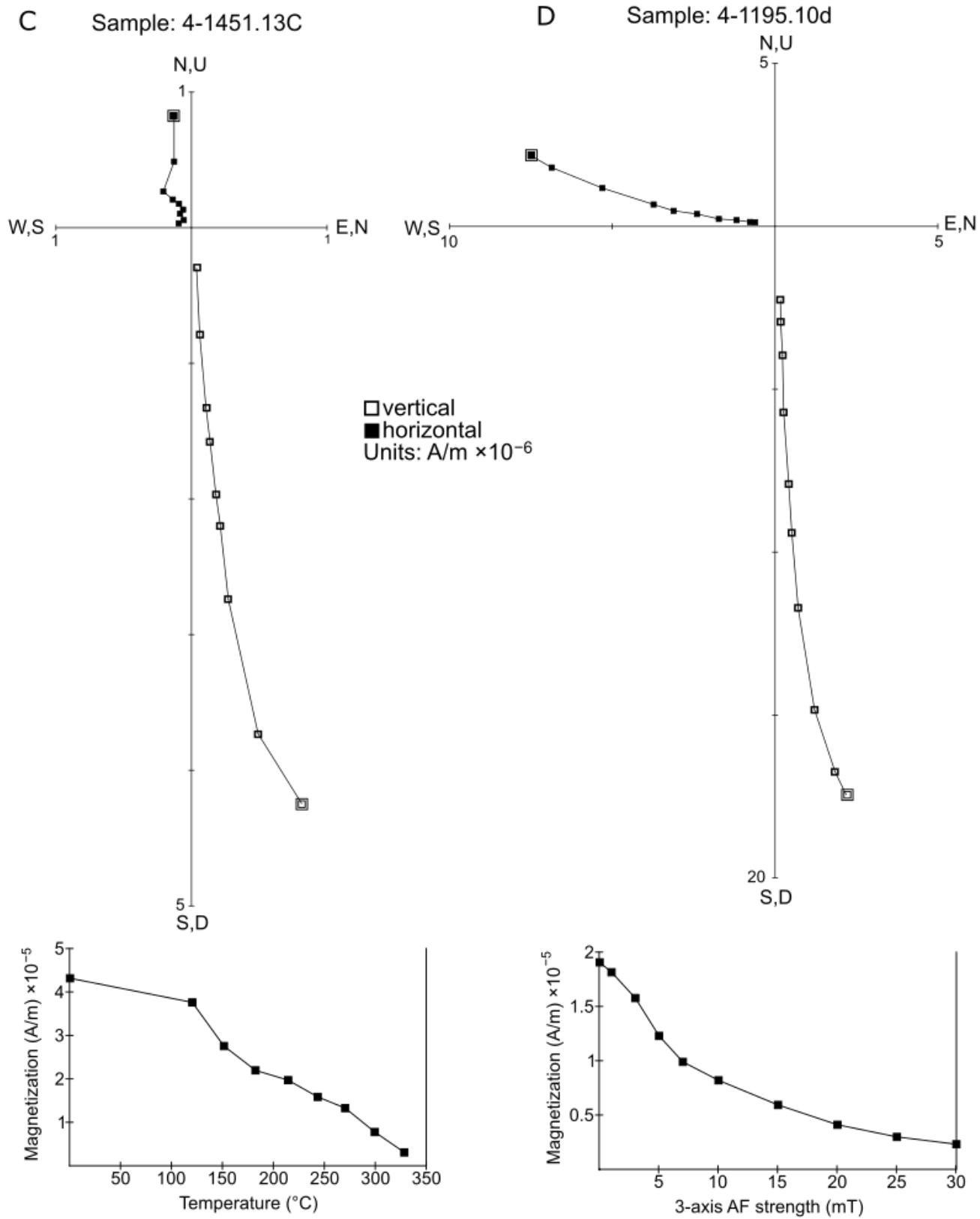


Figure 8. Continued.

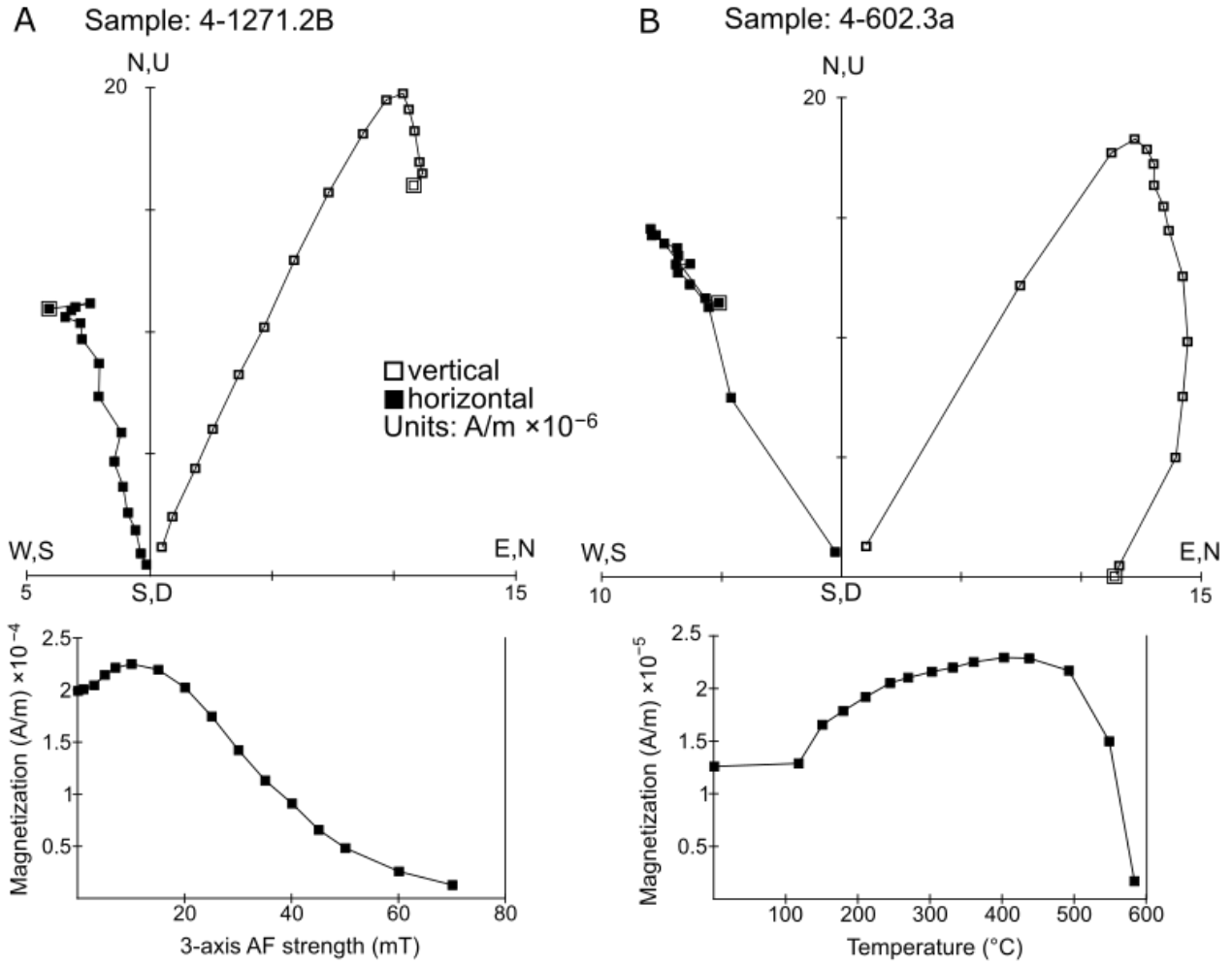


Figure 9. Zijderveld plots and demagnetization curves for representative components within the basalt lithology.

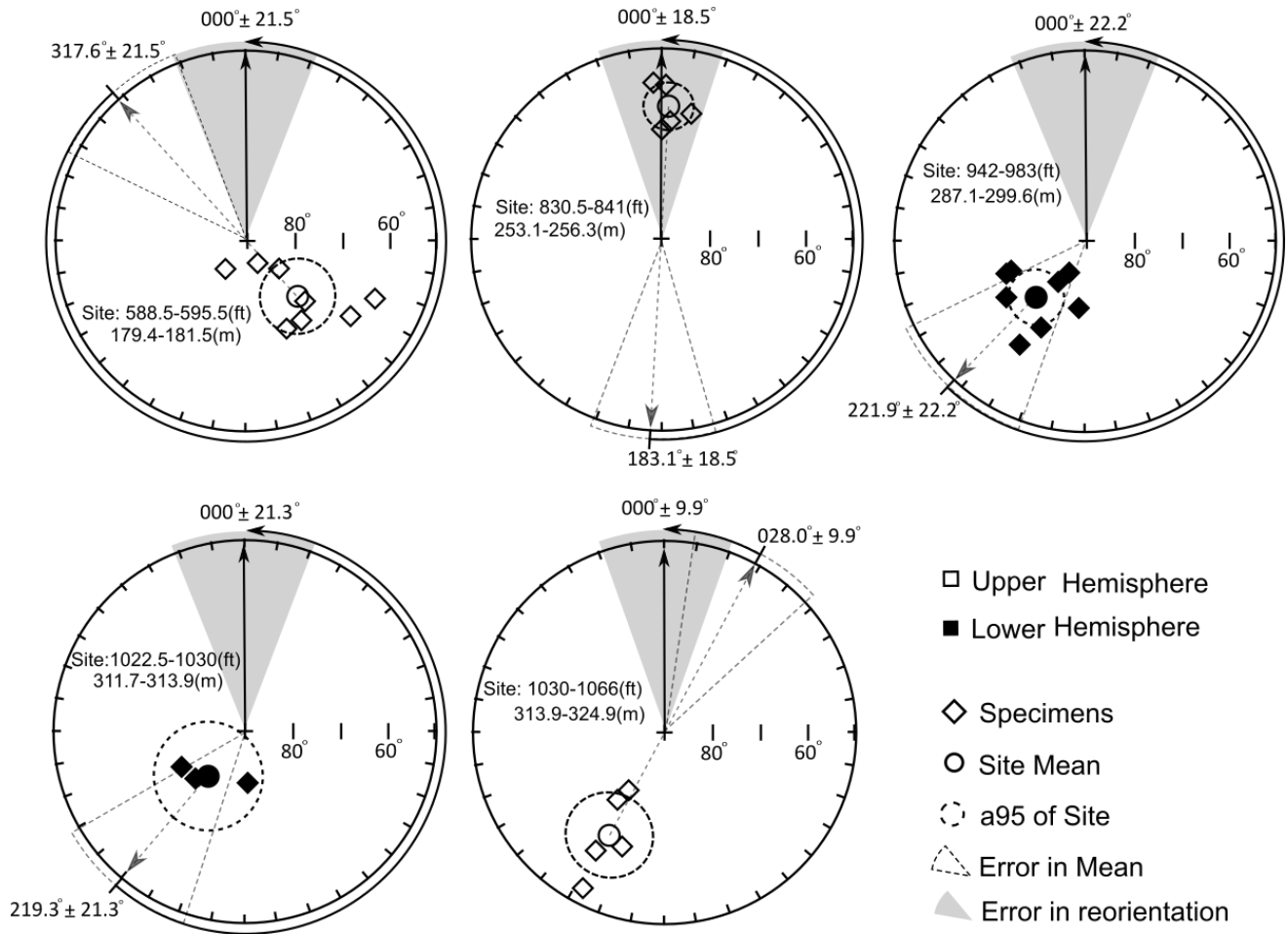


Figure 10. Site means (filled and hollow circles) of paleomagnetic directions (filled and hollow diamonds) and their reorientation error (dotted wedge outline) as calculated by Equations 1-3. The reorientation error is passed on to structural data (solid gray wedge) as the site means are rotated back to geographic north. The α_{95} of each site is marked by a dashed circle. Note that stereonets are cut off at 50° plunge to show detail.

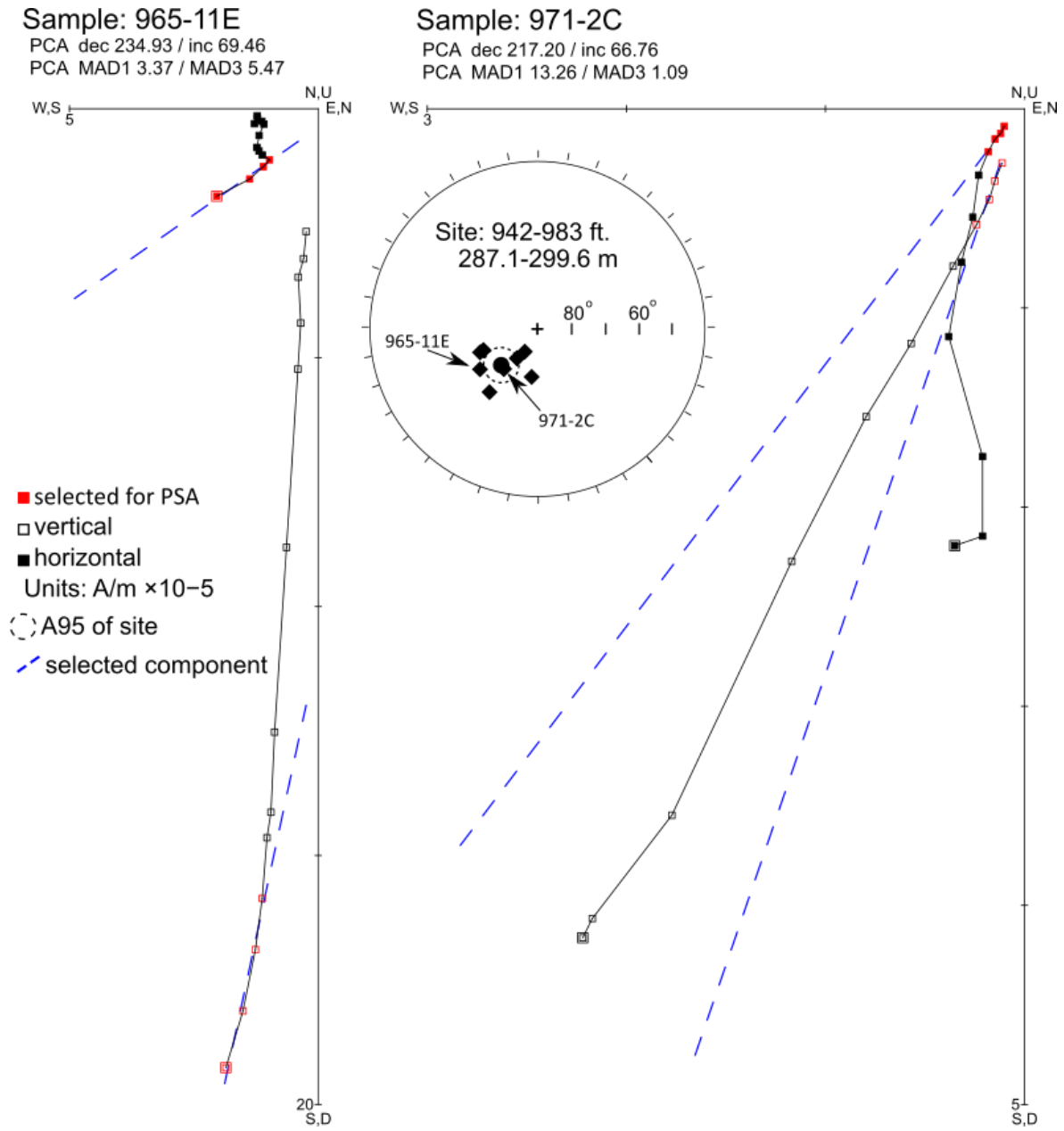


Figure 11. Zijderveld plots for specimens 965-11E (left) and 971-2C (right), and stereonet for the 287.1-299.6 m site (center). The first component of sample 965 aligns with the second component in the 971 sample. Selected components are outlined in dashed blue lines. Demagnetization steps that were selected for PSA analysis are red.

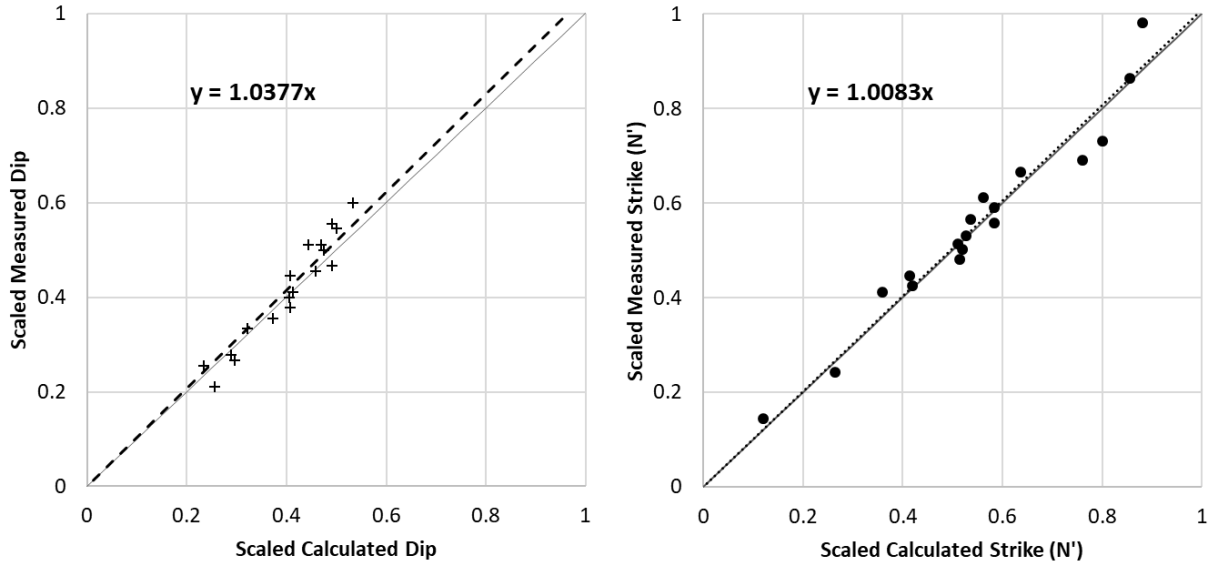


Figure 12. Comparison of calculated and measured dip (left) and strike (right) data. Data are normalized by 90 for dip data and by 360 for strike data. Trend lines have a y intercept set to the origin.

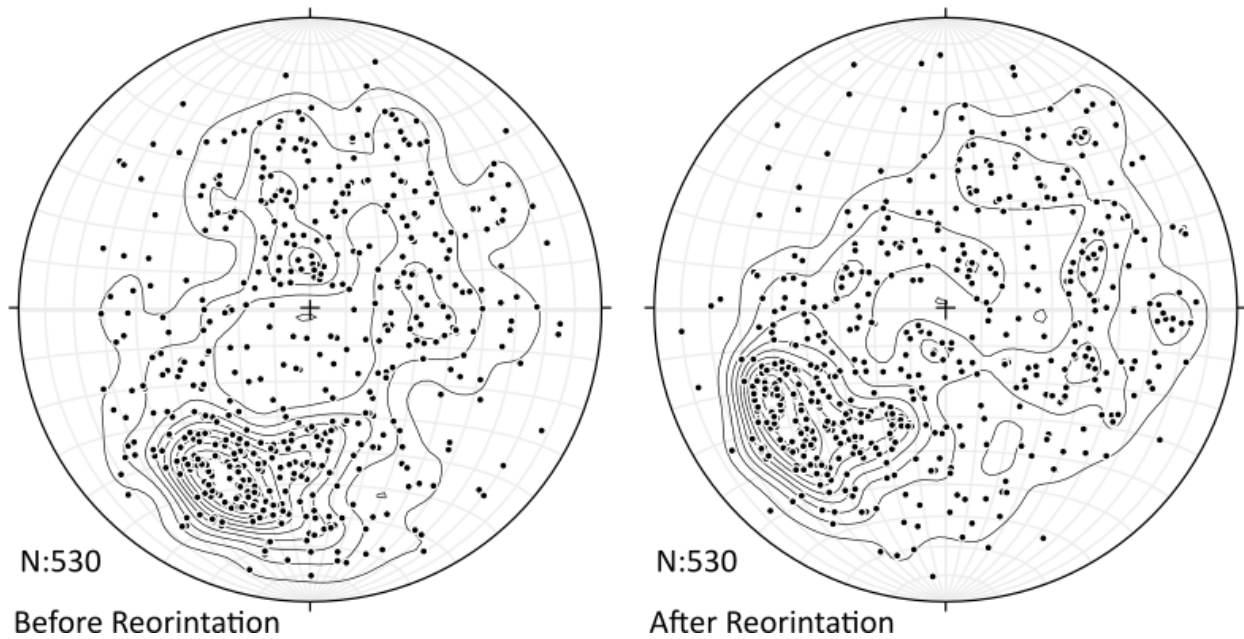


Figure 13. Poles to planes of structural features measured in the core before reorientation by paleomagnetic directions (left) and after reorientation (right). Kamb contours have a significance level of 3 sigma and an interval of 2. N indicates the number of measurements presented.

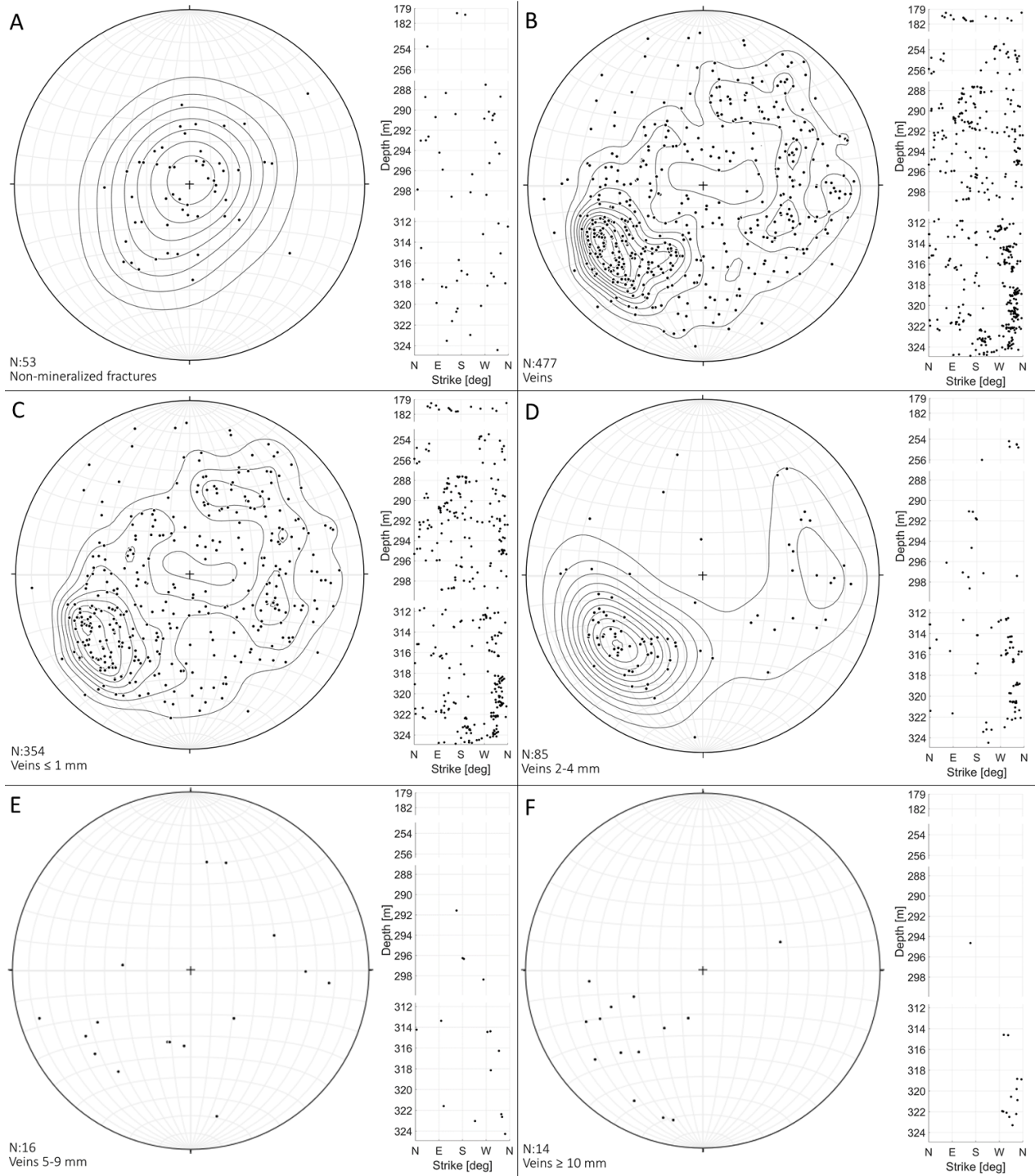


Figure 14. Stereonets of poles to planes and depth vs strike plots for veins that A) have no mineralization on the fracture, B) all veins, C) veins that are ≤ 1 mm, D) 2-4 mm, E) 5-9 mm, and F) > 10 mm in width. C-F are subsets of the data presented in B. N indicates the number of measurements. Kamb contours in the stereonets have a significance level of 3 sigma and an interval of 2. N indicates the number of measurements presented. Note the scale breaks on depth versus strike plots.

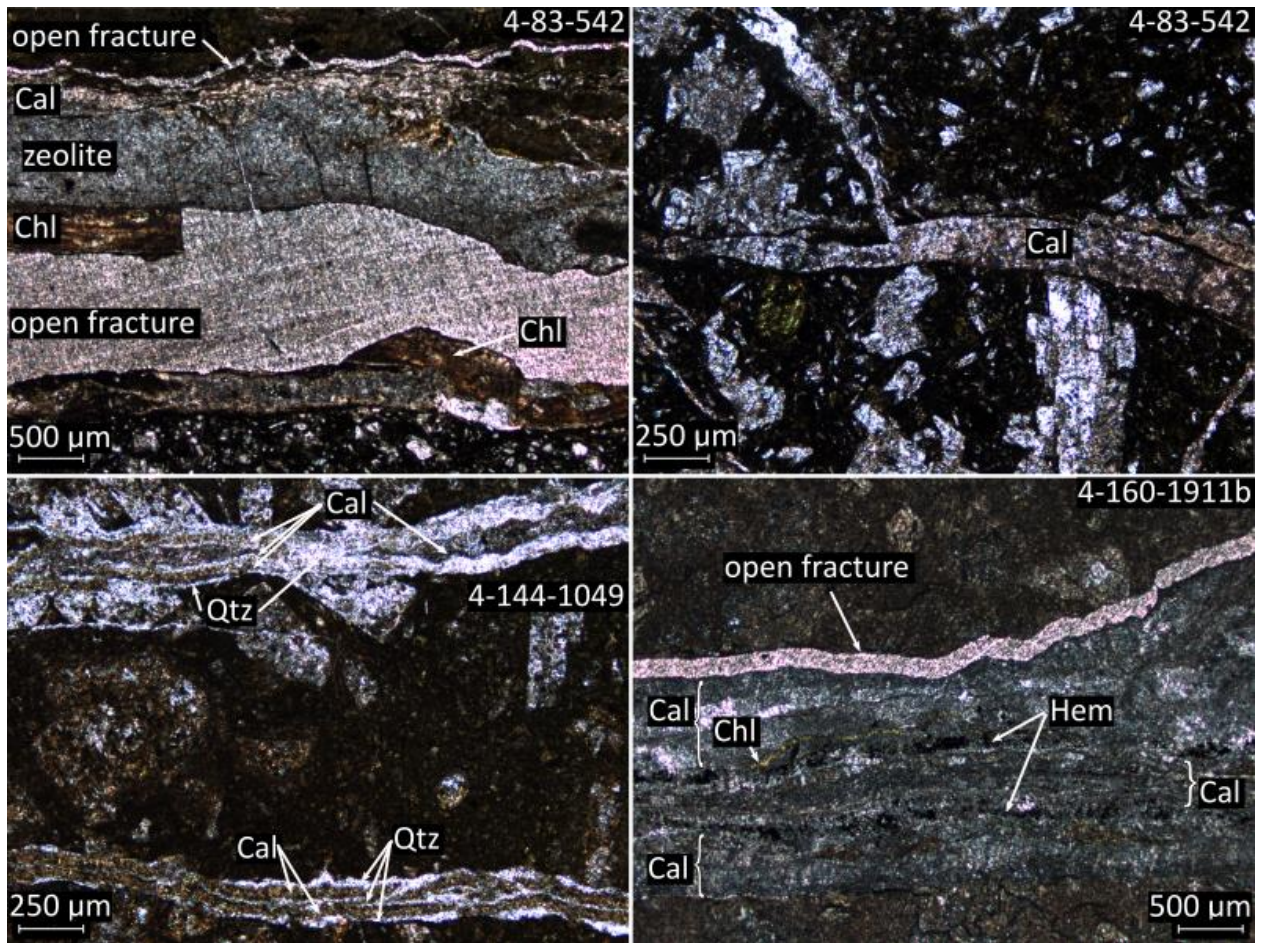


Figure 15. Micrographs taken in plain polarized light of monomineralic (4-83-542 top right) and polymineralic (4-83-542 top left, 4-114-1049, 4-160-1911b) veins within reoriented sections of the TG-4 core. Polymineralic veins show evidence of crack-seal mineral growth in the form of symmetrical mineral laminations in 4-144-1049 and 4-160-1911b, and vein material on either side of an aperture in 4-83-542 (top left). Cal=calcite, Chl=chlorite, Hem=hematite. Host rock in each image is black to dark brown with phenocrysts of plagioclase.

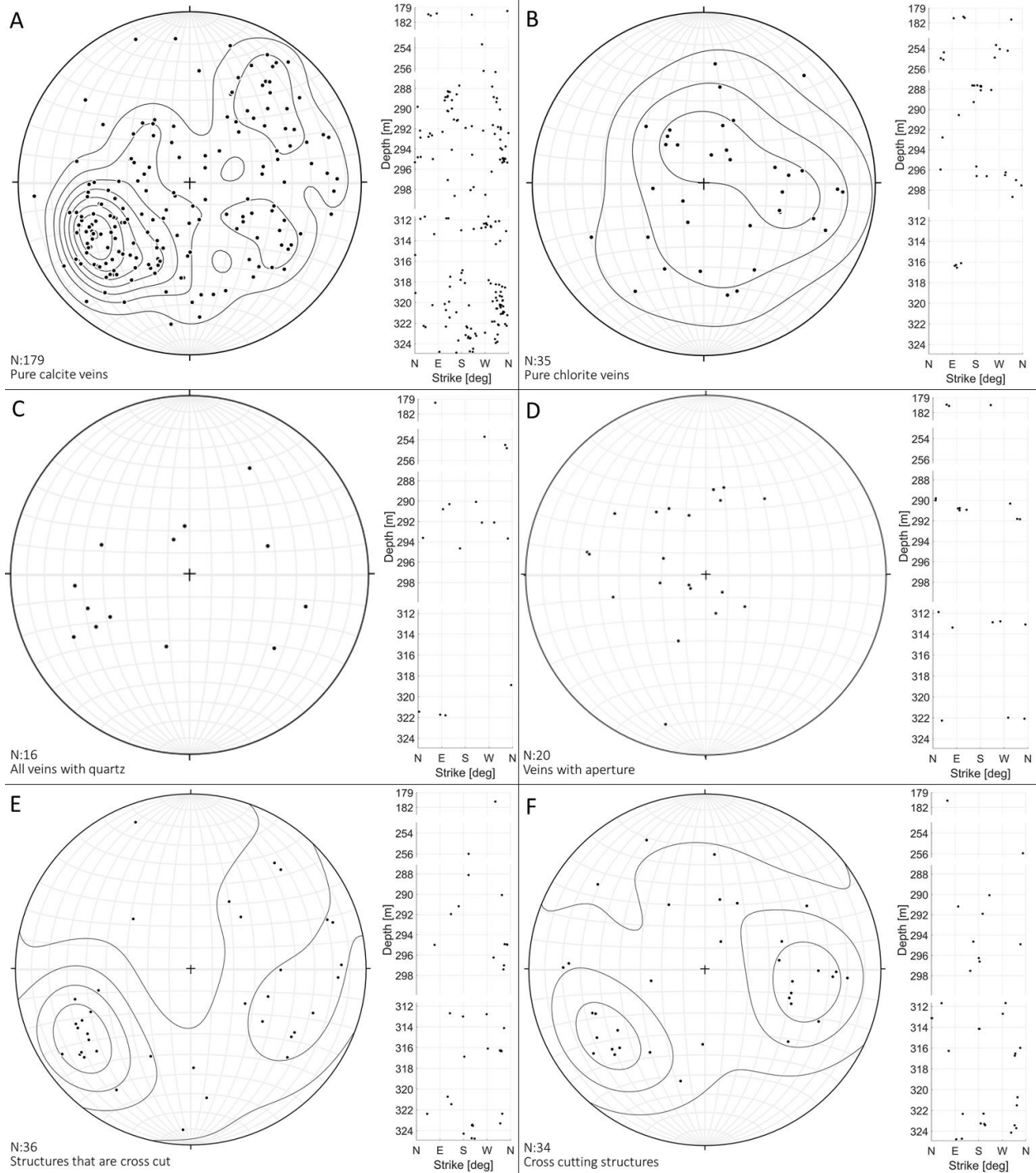


Figure 16. Stereonets of poles to planes and strike vs depth plots for veins that are filled with A) only calcite, B) only chlorite, C) quartz, D) partial mineralization with aperture, E) structures that are cross cut (i.e. the ‘older’ generation of veins) F) structures that are cross cutting other (i.e. the ‘younger’ generation of structures). All data are subsets of the data presented in 13.B. N indicates the number of measurements presented. Kamb contours on the stereonet have a significance level of 3 sigma and an interval of 2. Note the scale breaks on depth versus strike plots.

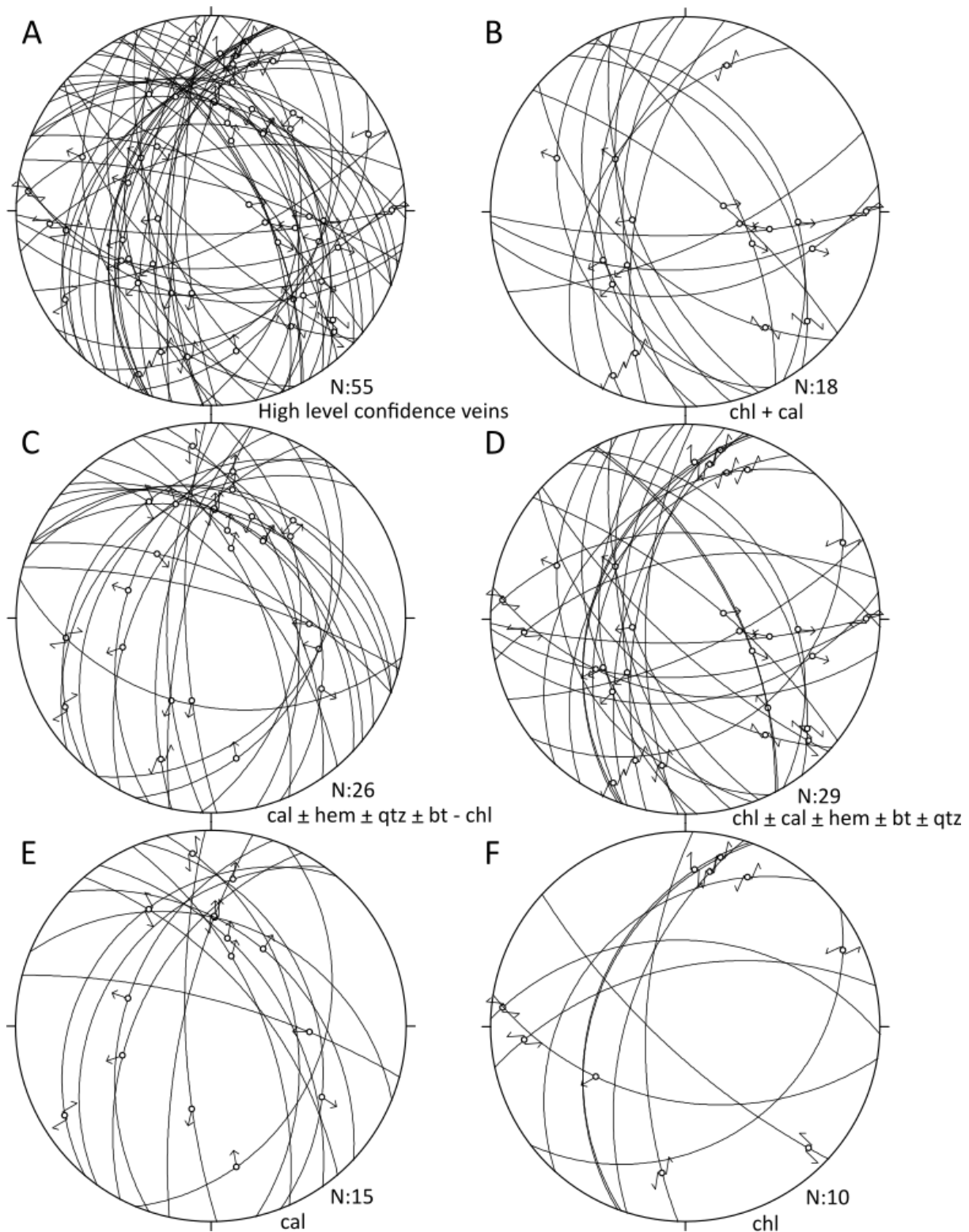


Figure 17. Stereonets showing the orientation of shear veins (great circles) and relative movement of the hanging wall (arrows) as indicated by the slickenline rake (small circles) for A) shear veins with high confidence slickenfibers, and B-F) sub-sets of A separated by mineralogy. Calcite=cal, chlorite=chl, quartz=qtz, hematite=hem, biotite=bt. N= number of structures plotted.

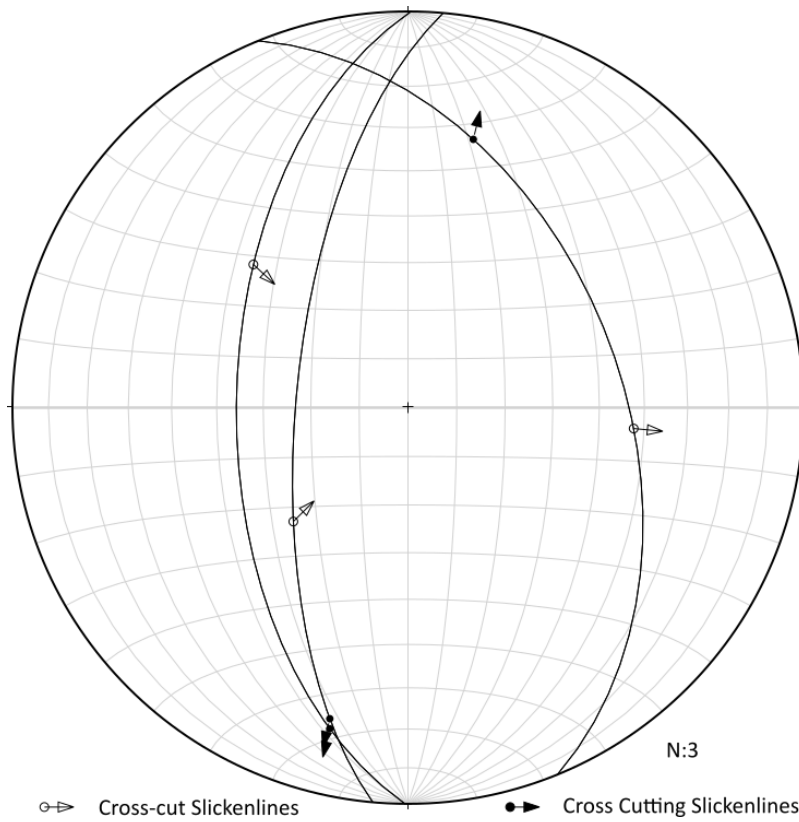


Figure 18. Shear veins with multiple slickenlines. Arrows point in the direction of hanging wall movement as indicated by slickenlines. Cross cutting slickenlines are indicated by filled arrows and cross-cut slickenlines are marked by hollow arrows.

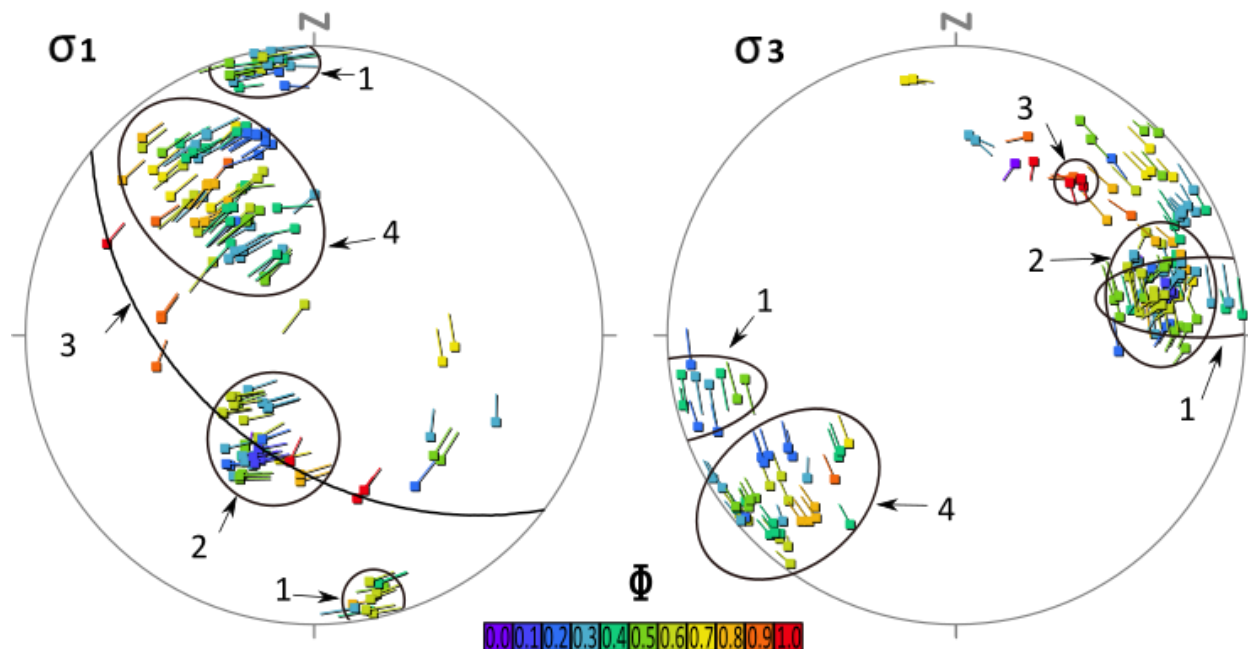


Figure 19. Results of MIM analysis for high-confidence shear veins. Orientation groups are circled in black. See text for orientation group descriptions. Sigma 1 directions are plotted on the left and sigma 3 directions are plotted on the right. Squares indicate directions and the line extending out of each square points in the azimuth direction of the paired direction in the other plot. Longer lines indicate a paired direction with a shallower plunge. All orientations have a directional error of $\pm 20.7^\circ$. The error on the plunge can be estimated by the vertical spread of each solution cluster. Colors indicate the Φ value with purple = 0.0 and red = 1.0. Dispersion factor = 2 and enhancement = 10.

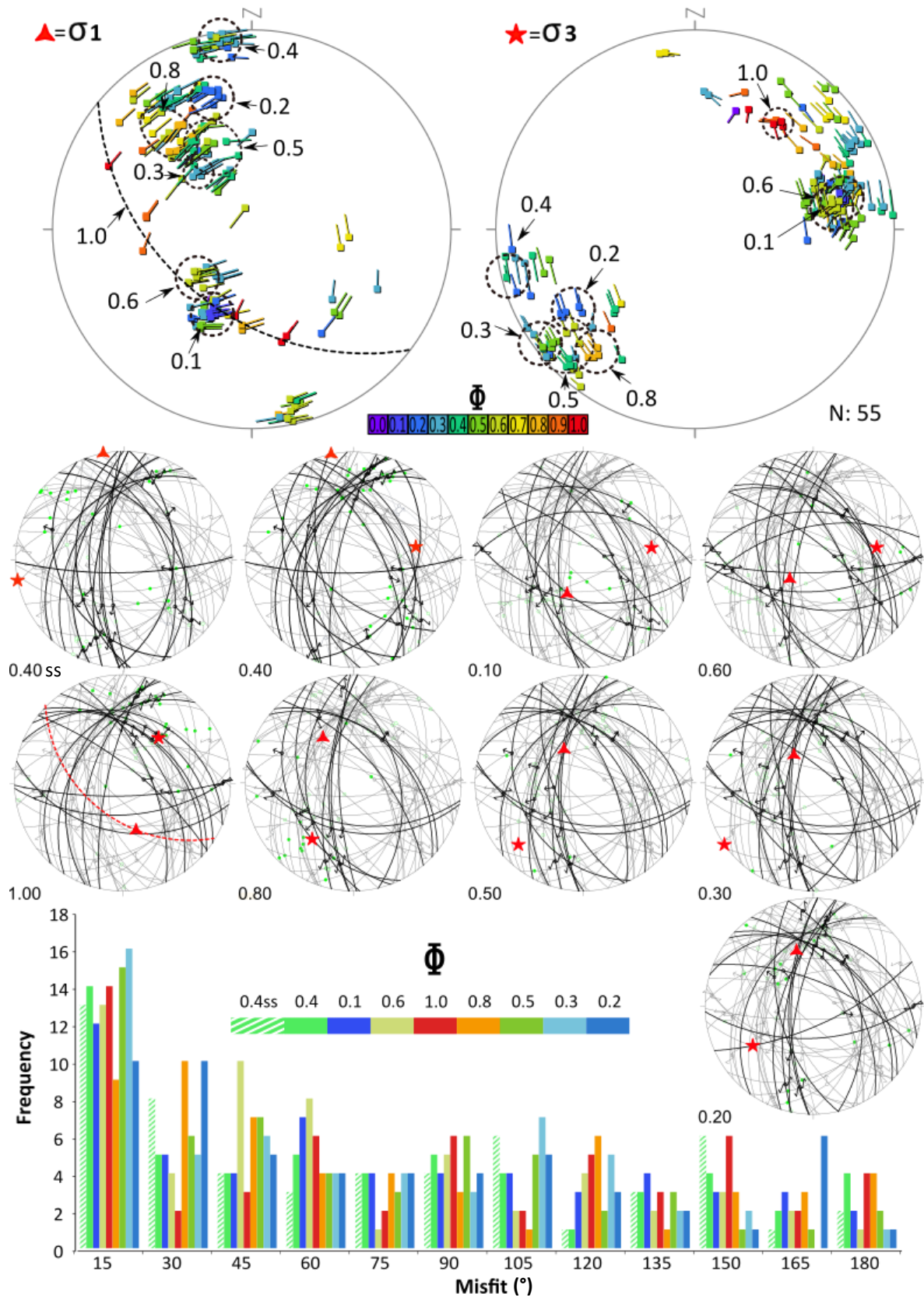


Figure 20. Results of the multiple inverse method (MIM) on all high-confidence shear veins (top, see Figure caption 19 for explanation). Dashed lines demarcate solution clusters picked for error analysis. The numbered arrows pointing to each cluster are the Φ values picked for that cluster. N= the number of samples. The small stereonet (central) show shear vein orientation (great circles) and slickenline movement indicators (arrows on the great circles) of the hanging wall. The number below and to the left of each stereonet corresponds to the Φ value of the solution cluster picked from the MIM results (top). 'ss' after the Φ value = strike slip. Black orientation data have movement indicators within 30° of the theoretical movement for that fault orientation, given the principal stress directions (σ_1 = red triangle, σ_3 = red star) and Φ value picked (i.e. the misfit). Gray orientation data have misfits $>30^\circ$. Bright green circles denote theoretical movement given fault orientation, principal stress directions, and Φ value. The histogram (bottom) compares the misfits of each solution. Bin size = 15° .

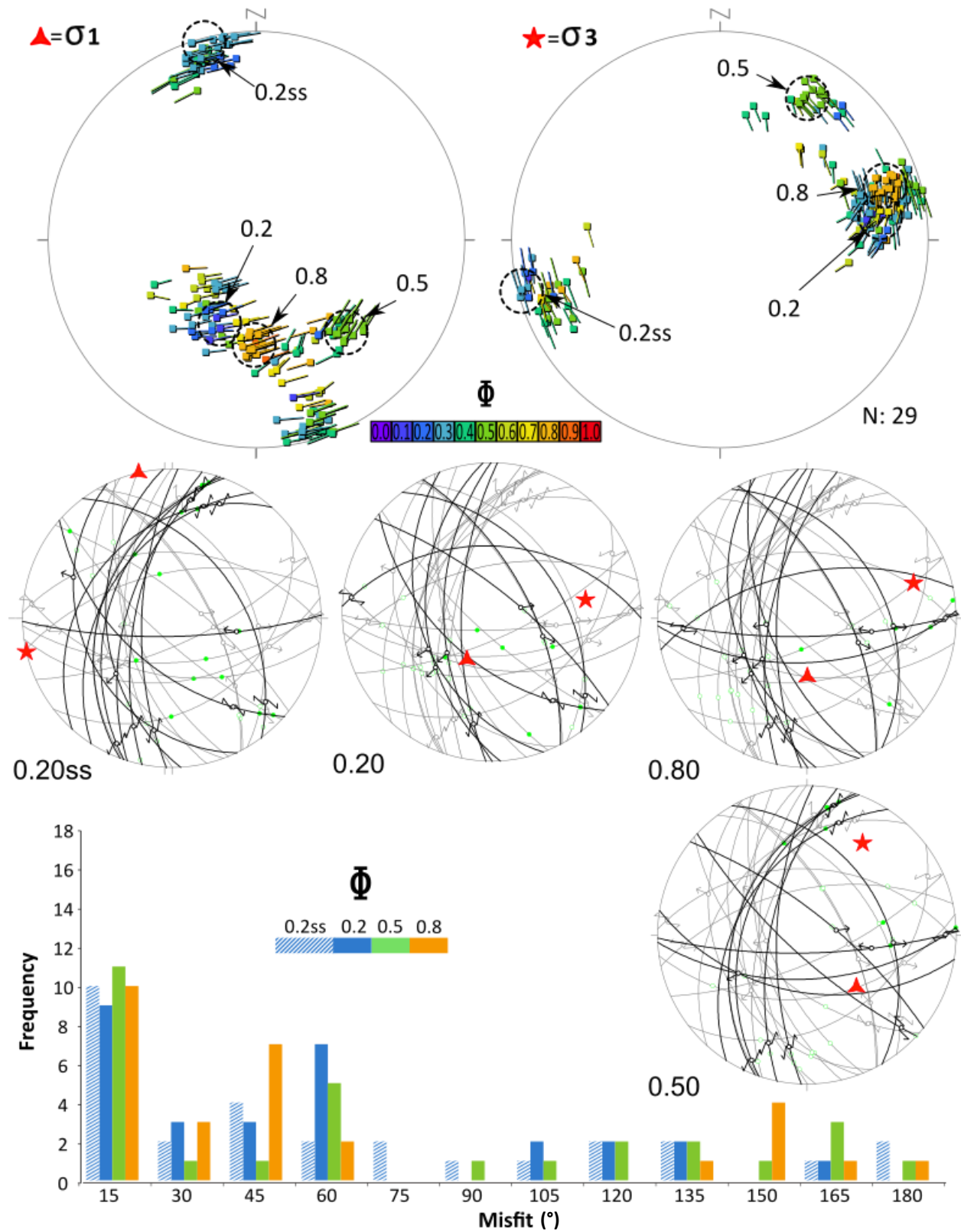


Figure 21. MIM results for all chlorite \pm calcite \pm hematite \pm biotite \pm quartz filled shear veins. See figure caption 20 for explanation.

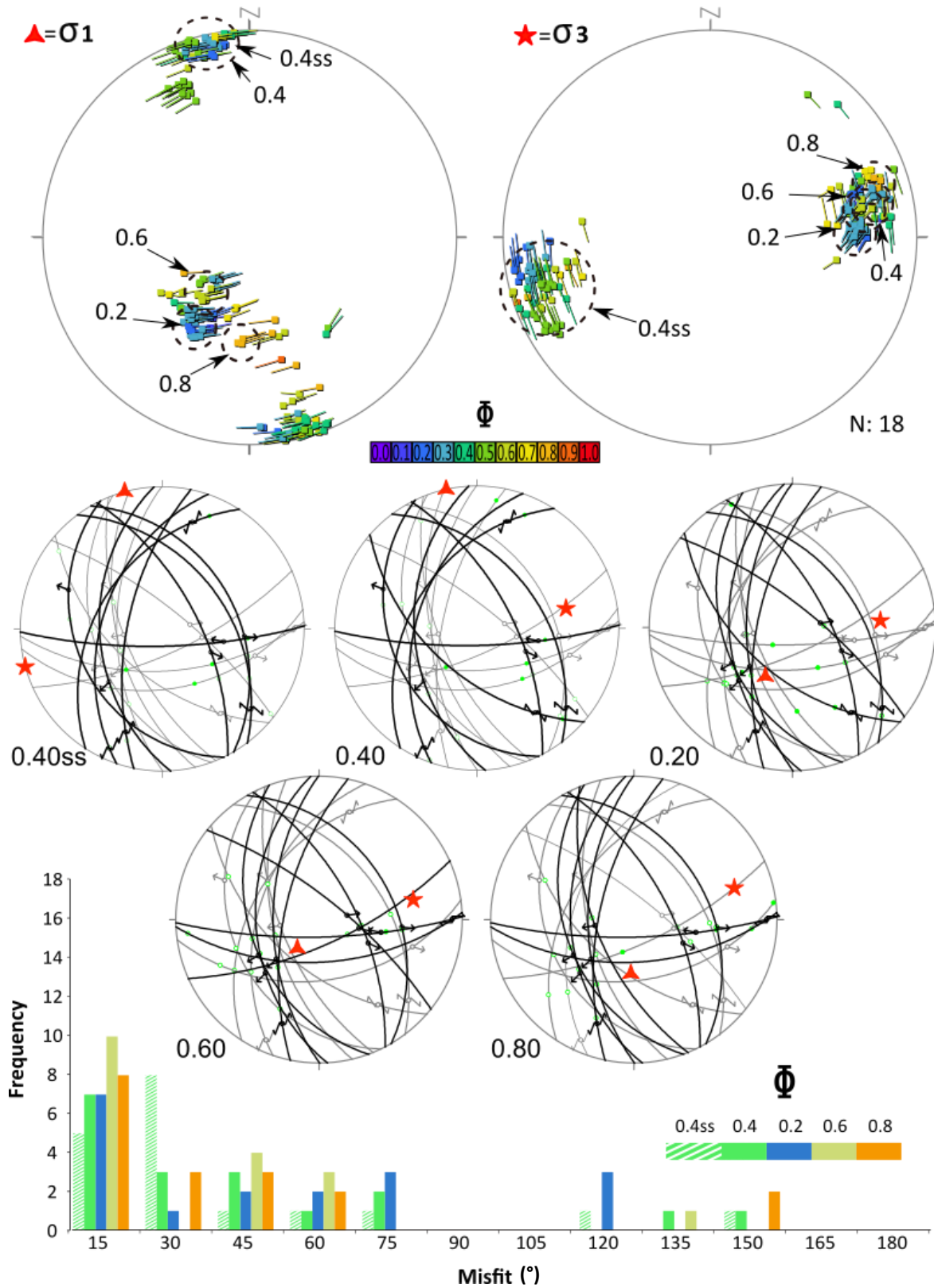


Figure 22. MIM results for all chlorite + calcite filled shear veins. See figure caption 20 for explanation.

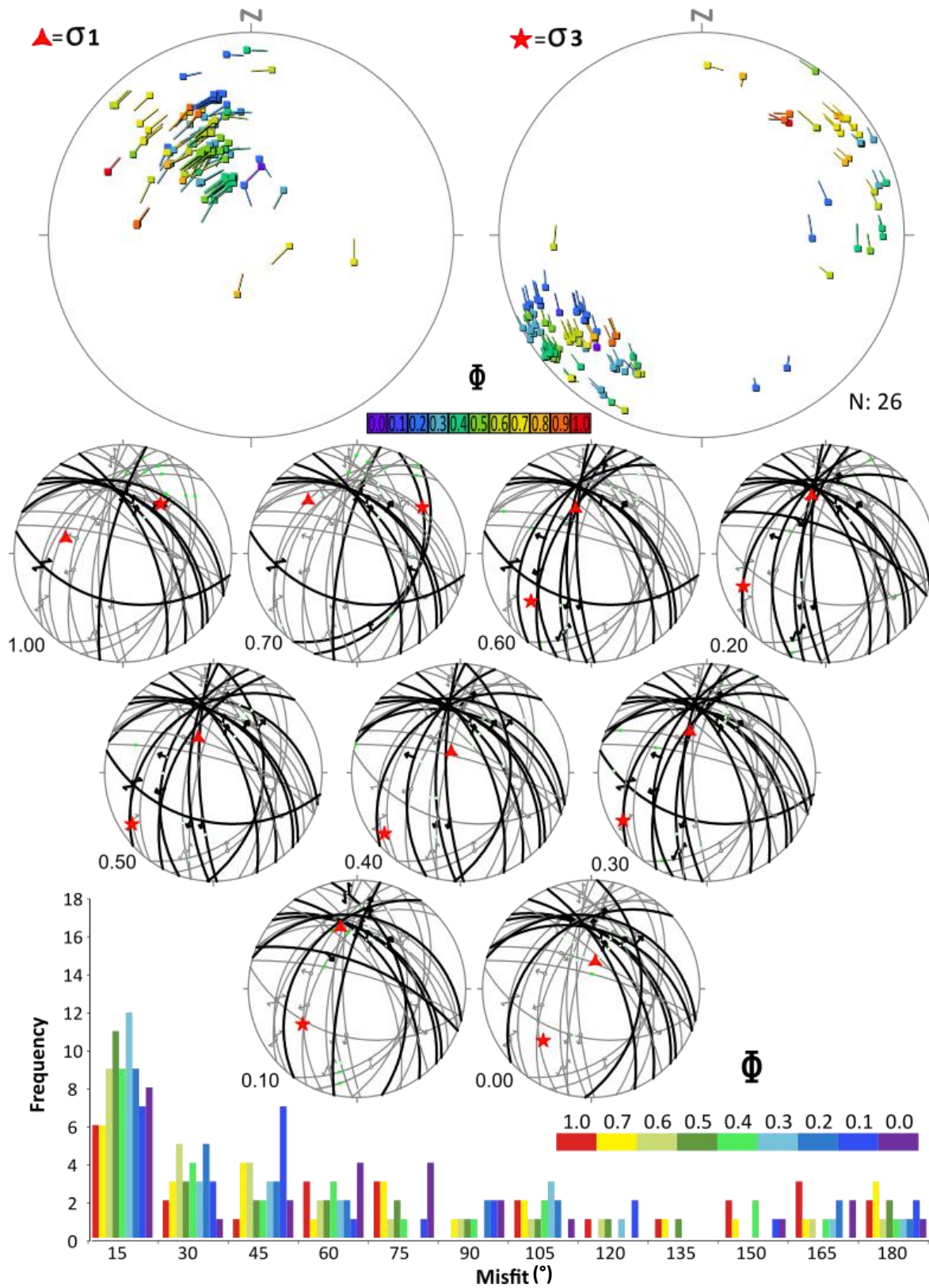


Figure 23. MIM results for all calcite ± hematite ± biotite ± quartz - chlorite filled shear veins. See figure caption 20 for explanation.

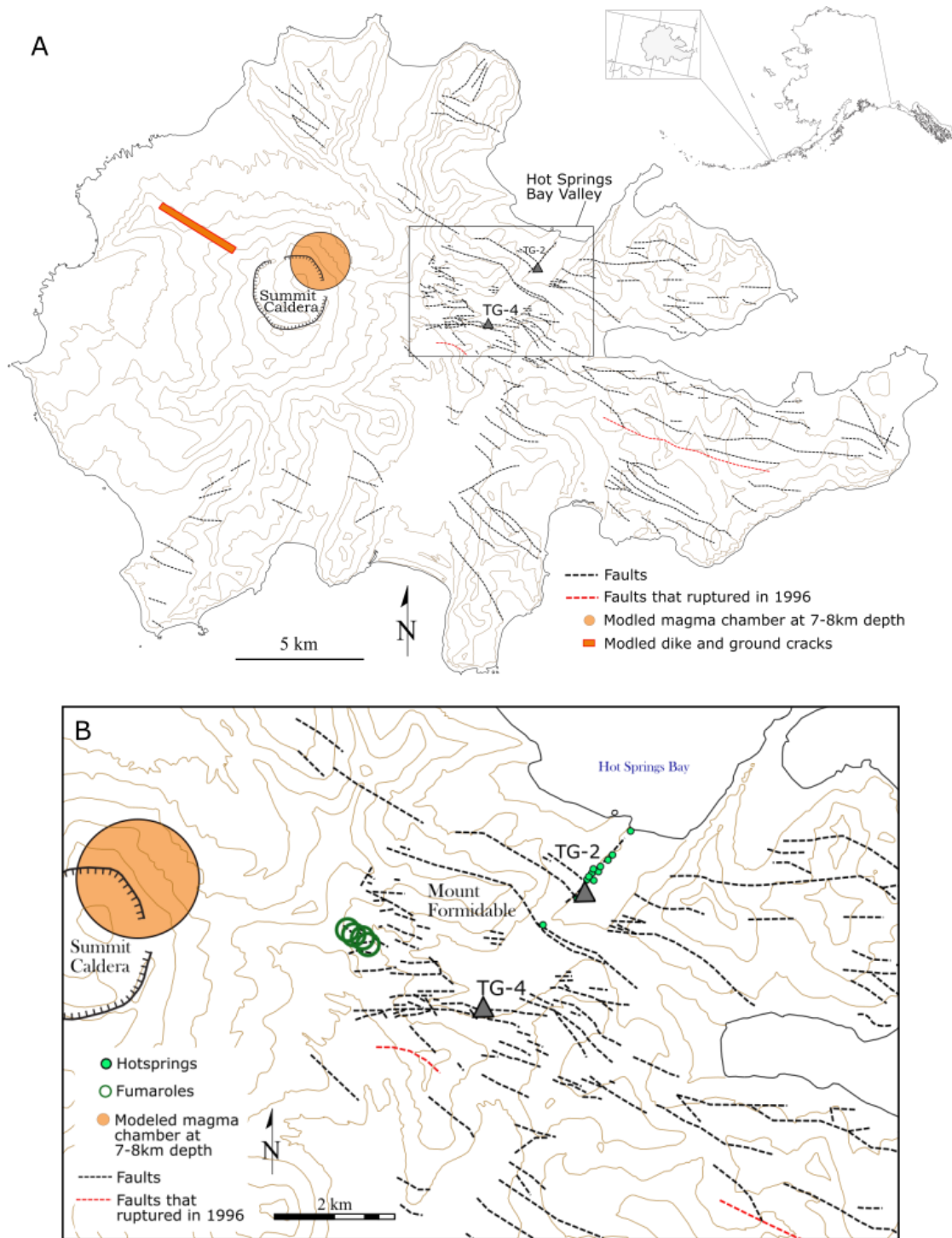


Figure 24. A) Map of Akutan showing mapped faults (dashed lines) (Stelling et al., 2015) in relation to the TG-4 well site, ground cracks and the modeled dike intrusion (orange rectangle)(Lu et al., 2005). Orange circle represents the modeled mush zone at 7-8km depth of (DeGrandpre et al., 2017). Elevation between topographic lines (brown) is 500 ft. (Richter et al., 1998). B) Inset map of Hot Springs Bay Valley shows the relation of well TG-4 to mapped faults and geothermal surface expressions such as fumaroles (hollow green circles) and hot springs (solid green circles).

Appendix A

A1. Rock Magnetism

A1.1 Sample Preparation

Samples were powdered with a marble mortar and pestle and placed in plastic pill casings; these were pressed onto the end of the sample holder. Chip samples were adhered to the sample holder with a silicone gel.

A1.2 Hysteresis

To create the hysteresis loops, samples were exposed from a zero field to a 1T field in 250mT steps. The direction of the field was then switched, and the magnetic moment of the sample was measured by the VSM. The magnetic moment is plotted vs. the strength of the field in Figure 2. Magnetic saturation (M_s) is the moment that a sample has when all the available magnetic domains have been aligned. M_s is visible in the hysteresis loops as the horizontal signal at high fields. It is important to note that the M_s is measured in the presence of a magnetic field. The magnetic remanence (M_r) is the moment that the sample has when the field is returned to zero. M_r represents the highest possible moment that the sample could retain in nature and is read off the vertical axis on the downward curve. The Magnetic coercivity (H_c) is the maximum field that a material can withstand without becoming magnetized, or demagnetized. H_c is read off the hysteresis loop where the loops crossed the horizontal axis. All these parameters are inputs in the Day plot (Figure 4), which is used to distinguish the domain states of the minerals present.

A1.3 Induced Remanent Magnetization (IRM)

The IRM curves are a measure of the total magnetization a sample could possibly hold in nature, as opposed to the M_r which is measured in the presence of a magnetic field. The VSM was used to measure IRM in the nine representative chip samples. Samples were exposed to increasingly high fields for 1 second, followed by a 0.5 second period of measurement in zero field.

A2. Demagnetization

A2.1 Sampling Method

Sample ID numbers are grouped in a hierarchy by locality, site, sample, and specimen. Each core is a locality, each run in the core is a site, each flow unit in that run is a sample, and each individual paleomagnetic cylinder drilled from the core is a specimen with the naming

scheme: (footage)-(piece number in the box)(specimen in sample). Six plug samples were drilled in each run that hosted an appropriate lithology. If the run had multiple lithologic units appropriate for sampling, three specimens were taken from each unit. A false north (N') was drawn along the length of each core run, and samples were drilled relative to the false north mark through the center of the core, so that the positive x direction on each specimen is parallel to N' and in the up-core direction (Figure 5). Specimens were cut using a diamond tipped band saw to obtain a cylinder 22 mm high and 24.7 mm in diameter from the center of the core. The plug samples were taken from the center of the core to minimize any drill induced remagnetization that could have affected the outside of the core, as suggested by Pinto and McWilliams (1990). When the plug samples were drilled out of the core, the up-core direction was alternated between north and south every other sample. This was done so that any magnetization the samples might pick up due to drilling in the present field is averaged out when the group of samples is taken as a whole. Similarly, when the plug samples were cut with the diamond saw, one side was cut with the z direction pointing up and the other side was cut with the z direction pointing down.

A2.2 Measuring AMS

The anisotropy of magnetic susceptibility (AMS) was measured with the Kappa Bridge in the PNWPL. The 'sampling angle' was set to 0 degrees' azimuth and 90 degrees down from vertical (hade) for all specimens, resulting in horizontally-drilled samples throughout the core. Because the declination of the runs was unknown prior to analysis the azimuth of the sample, the false north mark was defined as 0 degrees.

A2.3 Alternating Field Demagnetization

Half of the specimens from the samples with six specimens and all the specimens from the additional samples were demagnetized with increasing alternating field strength in the D-Tech 2000 AF (de)magnetizer. After the first demagnetization at 1 mT the field was increased to 2.5 mT and increased in steps of 2.5 until 10 mT. From 10 to ~40mT the demagnetization steps were 5 mT. 10 mT steps were used from ~40 mT until the sample had <10% of its original magnetization. For each demagnetization step the samples were placed in the alternating field with each axis parallel to the field. The order in which the axes were demagnetized varied with each step so that any acquired magnetization was averaged out. Specimens with high magnetic moments were measured on the spinner magnetometer and all other samples were measured on the 3-axis 2-G Enterprises model 755 cryogenic magnetometer. See Table 1 for reference.

A2.4 Thermal Demagnetization

A common occurrence in thermally treated rocks is the growth of goethite (FeOOH) and hematite (Fe₂O₃), which can obscure the true magnetic signal of a material. These minerals produce a softer signal than primary minerals such as magnetite (Fe₃O₄) so it is therefore unlikely that the signal will be completely overprinted. However, due to the limited number of available sampling sites, secondary mineral growth was tested. To this end, a pilot study was done to test the effects of heating in the presence of free oxygen. Two identical sets of specimens were selected from the core; all lithologies were represented. The first set of specimens were demagnetized in air and the second were demagnetized in an Argon atmosphere. There are two ovens in the PNWPL; the TD48 (upper) oven and the TD48SC (lower) oven, the latter of which has atmospheric controls. The magnetic field inside each oven can be measured with the digital magnetometer model DM 2220 and if it is higher than ~0.02 mT the oven should be demagnetized. This is done by passing an alternating field through the coils. The field is slowly ramped up to and down from 40 volts; the process is repeated three times. Argon was used to cool the specimens in the lower oven until they reach 300 °C, after which air was used to cool until the specimens could be handled. The temperature steps start at 120 °C and increased over 17 steps of 30 °C increments until the sample reached 600 °C. Between each thermal step the magnetic susceptibility and remanence were measured on the Bartington and cryogenic magnetometers, respectively. Any difference in the susceptibility trends between the two sets of specimens indicates growth of magnetic minerals. No significant difference was observed between the set demagnetized in air and the set demagnetized in argon, therefore mineral growth due to oxidation is not a significant enough effect on the magnetic remanence to warrant demagnetization in Argon. Following the results of the thermal test the rest of the specimens from the six specimen samples were demagnetized in the upper oven in air.

A3. Core log Creation

A3.1 Image Collection

Each selected core run was photographed with a Nikon COOLPIX B500 digital camera. The core segments were placed on a rack with a green screen background. The green screen was connected on both ends to two dowels that could be rotated, in this way when the green screen was rolled up on the dowel it rotated the core which was resting on it. This set up allowed for images to be taken at all angles around the core segments. The quality of the model produced is directly

related to the quality of the images inputted. Images need to be in focus and with at least 50% overlap, taken at varied focal lengths and angles. For this work I found that taking images around the circumference and length of the core in a ‘zig-zag’ pattern as well as orthogonal to the core produced the best results. The images taken in a ‘zig-zag’ pattern around the core maximized the degree of curvature able to be reconstructed and the images taken orthogonal to the length of the core kept the model from being curved around an axis perpendicular to the length of the core, as often happens when images taken at low angles to the subject are used in the reconstruction.

A3.2 Masking

Masking can be done by hand in the Agisoft PhotoScan software. This is, however, time consuming and tedious. A python script written by Daniel Fagerlie, a computer science undergraduate student at Western Washington University, was used to automate the process. The script identifies all the green pixels in an image and classifies them as black. The rest of the image is classified as white. An additional algorithm is used to smooth the boundary between the black and white pixels, and finally the image is saved with the file name *original image name_mask.png* in a folder of the users choosing.

A3.3 Agisoft PhotoScan Workflow

The fundamental Agisoft workflow is well established. The images were loaded, masks imported, photos aligned, and dense point clouds generated with the batch processing tool. The software is capable of stitching ~4 feet and 30 degrees of core together at a time. The unaligned photographs were moved to a new workspace, called a ‘chunk’ in the Agisoft software, and processed to the dense point cloud stage. This was repeated until the entire core was represented, albeit in separate chunks. Markers were manually placed on reference points on models in different chunks and the “align by marker” and “merge chunks” tools were used to stitch the model segments together. Once combined, the ball-and-stick model and texture were generated with the batch processing tool. Before the orthomosaic was created the bounding box was reduced to just fit the model with the positive z direction pointing up-core. The orthomosaic was created using a cylindrical projection using the current region setting. This way the axis of the projection is parallel to the axis of the core. The 2-dimensional projections of the textured model were exported as .PNG files.